Cell Reports

Article

Mutations from patients with IPEX ported to mice reveal different patterns of FoxP3 and Treg dysfunction

Graphical abstract

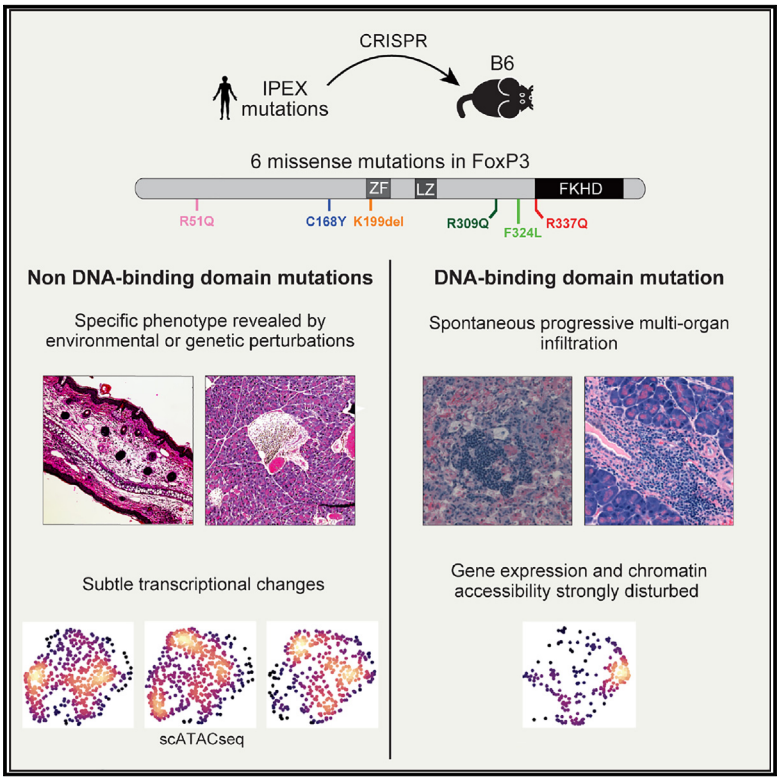

Highlights

- A panel of 6 FOXP3 mutations from patients with IPEX CRISPRed into the mouse germline
- Normal Tregs profoundly alter phenotypes of mutant Tregs by rescue and/or competition
- DNA-binding mutation induces a spontaneous multiorgan autoimmunity and high IgE
- Perturbations reveal organ-specific autoimmunity from N-terminal IPEX mutations

Authors

Juliette Leon, Kaitavjeet Chowdhary, Wenxiang Zhang, ..., Sun Hur, Diane Mathis, Christophe Benoist

Correspondence

cbdm@hms.harvard.edu

In brief

Leon et al. show that IPEX FoxP3 mutations can split into two. A Forkhead domain mutation induces spontaneous multiorgan inflammation, while inflammatory or genetic challenges reveal organ-specific impacts of mutations outside the DNA-binding domain. IPEX heterogeneity results from the location of FoxP3 mutations as well as from genetic and environmental perturbations.

Leon et al., 2023, Cell Reports *42*, 113018
August 29, 2023
https://doi.org/10.1016/j.celrep.2023.113018

CellPress

Cell Reports

CellPress
OPEN ACCESS

Article

Mutations from patients with IPEX ported to mice reveal different patterns of FoxP3 and Treg dysfunction

Juliette Leon,[1,2] Kaitavjeet Chowdhary,[1] Wenxiang Zhang,[3] Ricardo N. Ramirez,[1] Isabelle André,[2] Sun Hur,[3] Diane Mathis,[1] and Christophe Benoist[1,4,*]

[1]Department of Immunology, Harvard Medical School, Boston, MA, USA
[2]INSERM UMR 1163, University of Paris, Imagine Institute, Paris, France
[3]Howard Hughes Medical Institute, Program in Cellular and Molecular Medicine, Boston Children's Hospital, Department of Biological Chemistry and Molecular Pharmacology, Harvard Medical School, Boston, MA, USA
[4]Lead contact
*Correspondence: cbdm@hms.harvard.edu
https://doi.org/10.1016/j.celrep.2023.113018

SUMMARY

Mutations of the transcription factor FoxP3 in patients with "IPEX" (immune dysregulation, polyendocrinopathy, enteropathy, X-linked syndrome) disrupt regulatory T cells (Treg), causing an array of multiorgan autoimmunity. To understand the functional impact of mutations across FoxP3 domains, without genetic and environmental confounders, six human *FOXP3* missense mutations are engineered into mice. Two classes of mutations emerge from combined immunologic and genomic analyses. A mutation in the DNA-binding domain shows the same lymphoproliferation and multiorgan infiltration as complete FoxP3 knockouts but delayed by months. Tregs expressing this mutant FoxP3 are destabilized by normal Tregs in heterozygous females compared with hemizygous males. Mutations in other domains affect chromatin opening differently, involving different cofactors and provoking more specific autoimmune pathology (dermatitis, colitis, diabetes), unmasked by immunological challenges or incrossing NOD autoimmune-susceptibility alleles. This work establishes that IPEX disease heterogeneity results from the actual mutations, combined with genetic and environmental perturbations, explaining then the intra-familial variation in IPEX.

INTRODUCTION

Immune dysregulation, polyendocrinopathy, enteropathy, X-linked syndrome (IPEX) is a rare and severe autoimmune disorder caused by mutations in the *FOXP3* gene, which perturb the homeostasis and function of regulatory T cells (Tregs). Patients with IPEX present with severe immune dysregulation and develop autoimmune diseases at a very young age, as do *Foxp3*-deficient *scurfy* mice. As *FOXP3* is located on chromosome X, patients with IPEX are hemizygous males, while heterozygous carrier females are protected by normal Tregs that coexist with cells that express the mutant allele.[1–3] Many IPEX-causing *FOXP3* mutations have been reported,[4,5] but IPEX remains a rare disease.

Our understanding of the mode of operation of FoxP3, a transcription factor (TF) of the Forkhead family, is unresolved at present. While it contributes to Treg function, it is neither necessary nor sufficient to establish Treg identity: Treg-like cells develop in the absence of FoxP3, and Treg-specific gene expression signatures comprise FoxP3-independent and -dependent modules.[3,6–10] Some have argued that FoxP3 is primarily a transcriptional repressor[11–15]; indeed, the repression of cytokines produced upon activation of conventional $CD4^+$ (Tconv) T cells, especially interleukin-2 (IL-2), is a well-established function of FoxP3. Conversely, several studies suggest that FoxP3 activates the majority of its target genes, with the difference between activation and repression being determined by the regulatory partners it coopts at each locus[7,16–19]. Further, it has been proposed that FoxP3 mostly functions indirectly, by regulating the expression of intermediate TFs like TCF1,[20] but we argued elsewhere that indirect control applies only to a minor segment of the Treg signature.[21]

IPEX includes enteropathy, dermatitis, and variable endocrine autoimmunity (primarily type 1 diabetes or thyroiditis) and, more rarely, autoimmune hepatitis, nephropathy, and cytopenias.[22–26] Disease typically begins in very young infants, prenatally in some cases, but other patients are diagnosed as adolescents. The range in IPEX clinical severity stems in part from the actual mutation, with complete loss-of-function (LOF) alleles being generally most deleterious while missense and small deletions are better tolerated.[27,28] But clinical manifestations and severity also vary widely between patients with the same mutation.[25] The variance may result from genetic modifiers that modulate the perturbed peripheral tolerance and its inflammatory consequences (severity in *scurfy* mice also varies with inbred backgrounds). However, immunological challenges and infectious history may also influence IPEX by tuning alternative tolerance pathways

and/or the degree of effector cell activation. Genetic modifiers and environmental elements are near impossible to ascertain in IPEX families, as the rarity of the disease precludes realistically powered genetic association or microbiome studies.

We recently used single-cell transcriptomics to analyze Treg dysregulation in a set of patients with IPEX and their relatives.[3] Every patient hosted Treg-like cells expressing the mutant FOXP3 protein. A monomorphic disease signature affected all $CD4^+$ T cells, whether Treg or Tconvs. This signature was cell extrinsic because it was extinguished by the presence of normal Treg cells in mixed bone marrow chimeric mice and in heterozygous mothers of patients with IPEX. We proposed that both aspects contribute to the pathology by compounding Treg dysregulation. The cell-intrinsic effects of each IPEX-causing mutation proved difficult to assess given the dominant cell-extrinsic perturbation, as well as the genetic and immunologic variables in each patient.

To circumvent these difficulties, and to analyze in a controlled manner the influence of genetic and environmental variables on the functional consequences of FOXP3 mutations, we used CRISPR germline editing to port into mice a panel of six *FOXP3* IPEX mutations. The results identify 2 different classes of IPEX mutations, objectify the importance of perturbations (genetic or inflammatory), and reveal an association between mutation location and specific disease manifestations.

RESULTS

Engineering mouse lines with FoxP3 missense mutations from patients with IPEX

The primary goal of this study was to examine, in a setting where genetic and environmental confounders are controlled, the genomic and immunologic consequences of IPEX-causing *FOXP3* mutations by introducing them into the genome of inbred C57BL/6J (B6) mice. We selected a panel of 6 IPEX missense mutations, mainly derived from our previous study of Treg genomics in patients with IPEX.[3] We eschewed complete LOF mutations, which cause full-blown *scurfy*-like disease and mutations in the DNA-binding domain that have been extensively analyzed,[29–32] and instead chose missense mutations that give rise to a range of pathologic and transcriptomic perturbations in patients[3] at positions conserved in the human and mouse FoxP3 proteins (Figure S1A). The mutations were spread across different domains of FoxP3 (Figure 1A): R51Q and C168Y in the N-terminal domain; K199del in the zinc finger domain; R309Q and F324L between the leucine zipper and Forkhead (FKHD) domains; and R337Q, located at the beginning of the FKHD and predicted to distinguish different conformations.[33] With regard to their clinical phenotype, patients from whom the mutations originated suffered from characteristic enteropathy, but several of them presented milder forms of the disease. All patients were still alive at last follow-ups, with ages ranging from 3 to 21 years, with two (K199del, R337Q) having required bone marrow transplantation[3,34] (Figure 1A; Table S1).

The mutations were introduced into the mouse genome by CRISPR-based mutagenesis via microinjection of editing complexes (Cas9 protein, gRNA, and ssDNA oligonucleotide for homology-driven repair) into the male pronucleus of fertilized oocytes. These oocytes derived from B6 females crossed to a Foxp3-GFP[36] male, aiming to introduce the mutations into a GFP-tagged *Foxp3* locus. However, this was achieved in only half the instances (Figure S1B), likely because the editing complex leaked into the cytoplasm and edited the B6-derived female pronucleus. For reference, we used a similarly generated mouse line bearing a frameshift mutation that eliminates the FKHD[19] (*Foxp3fs327-gfp*, hereafter KO [knockout]).

Founder animals with the desired mutations were identified by PCR and sequencing and were bred to expand and establish the lines. We have previously reported a preliminary assessment of R337Q.[33] All *Foxp3* exons were sequenced to verify the absence of adventitious mutations (Figure S1B). For experiments, the breeding strategy generated (1) heterozygous females in which the mutant allele was balanced by a wild-type (WT) allele (provided by a *Foxp3-Thy1.1* reporter); because of random chromosome X (ChrX) inactivation, such females contained both Treg-like cells expressing the mutant FoxP3 and normal Tregs expressing the WT allele; the latter ensured normal immunologic homeostasis (all heterozygous females healthy and fertile) and provided internal control cells in each mouse; and (2) hemizygous males expressing only the mutant FoxP3 and thus exposed to autoimmune manifestations, the equivalent of patients with IPEX (Figure S1C). Breedings were tailored to obtain experimental animals and sex-matched WT controls from the same litter (see STAR Methods; lines with mutations in the GFP-tagged or untagged alleles were controlled correspondingly; Figure S1C).

We first evaluated the expression of the mutant FoxP3 proteins *in vivo* in Treg-like cells from heterozygous females devoid of inflammation (Figure 1B). All mutant proteins were readily detected at levels equivalent to those of WT FoxP3, except for R337Q and K199del, which showed partially reduced levels (Figure 1C). These decreases did not result from interference with the epitope recognized by the anti-Foxp3 monoclonal antibody (mAb) used for detection (which binds a different sequence) and were confirmed with an alternative anti-FoxP3 mAb (Figure S1D). Tregs in all mutant lines showed largely normal levels of *Foxp3* mRNA (Figure 1D).

We also tested whether these mutations impacted FoxP3's DNA-binding ability. Proteins with these mutations were expressed *in vitro* (HEK-293T cells), with a C-terminal hemagglutinin (HA) tag. Extracts from these cells were used in pull-down assays, with a double-stranded DNA (dsDNA) oligonucleotide that contains an inverted repeat of the canonical TGTTTAC FKHD motif, which we recently showed to form a high-efficacy binding site for FoxP3 dimers.[33] The R337Q mutation led to a partial reduction in binding (Figure 1E), consistent with its position in the FKHD and with our previous results,[33] as did the neighboring F324L mutation, which might affect the domain-swapped conformation of FoxP3.[37] We also noted modest but reproducible reductions in DNA-binding activity for some N-terminal mutations. Overall, the mouse lines expressed mutant FoxP3 proteins at or near normal levels.

Differentiation and homeostasis of Tregs expressing the mutant FoxP3 proteins

To explore the functional impact of these FoxP3 IPEX mutations, we first assessed by flow cytometry their influence on Treg differentiation and homeostasis. To reveal the mutation's cell-intrinsic

CellPress
OPEN ACCESS

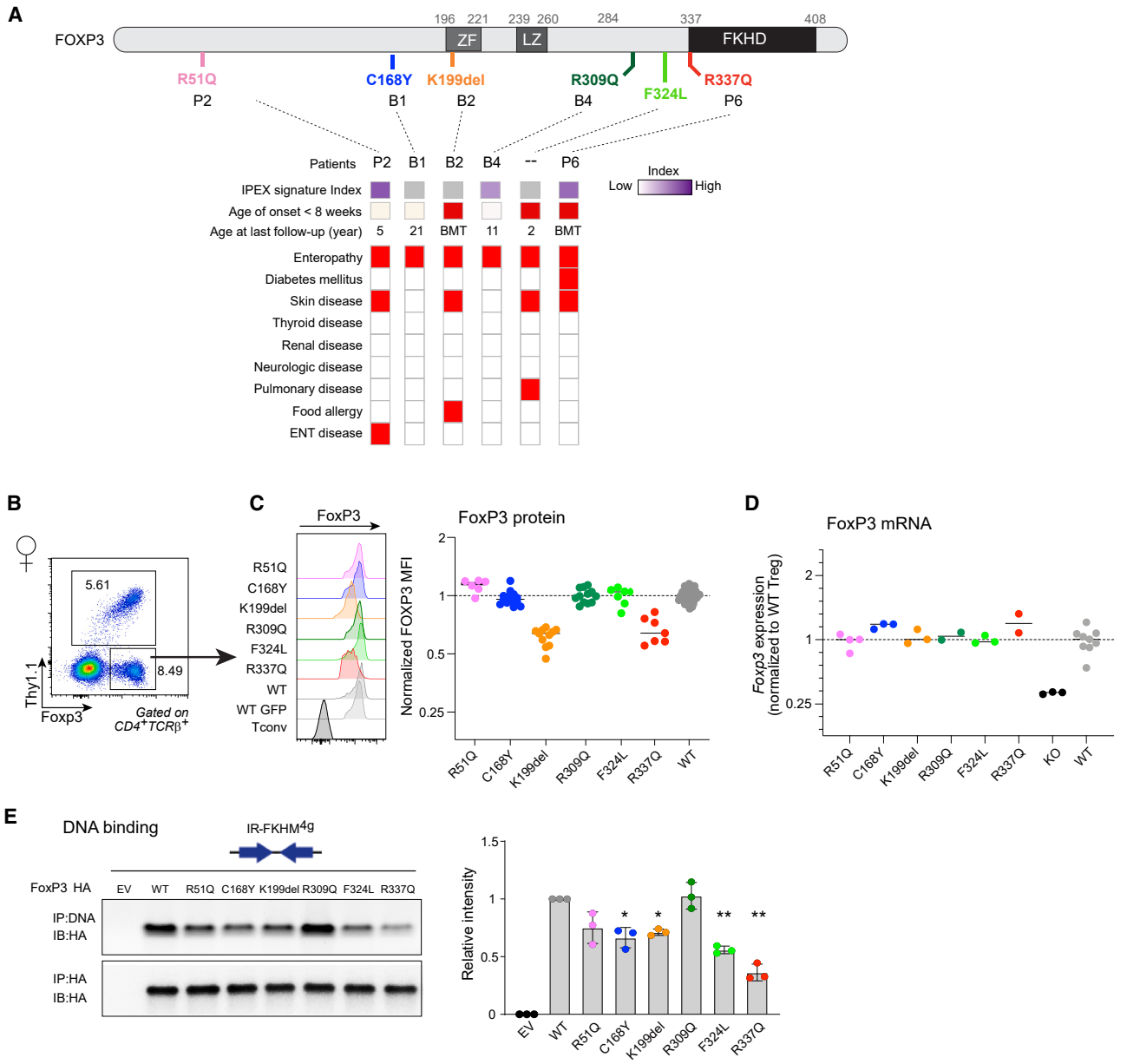

Figure 1. Selection and expression of mutant FoxP3 molecules

(A) Position of the engineered mutations into the mouse FOXP3 protein, and clinical characteristics of the human patients with IPEX from which they originate (coded as in Zemmour et al.,[35] except F324L, which is from Bacchetta et al.[34]). BMT, treated by bone marrow transplantation after sampling. Domains: ZF, zinc finger; LZ, leucine-zipper; FKHD, Forkhead. The "IPEX signature index" denoted severity by quantifying in Zemmour et al.[35] the transcriptomic disease footprint in CD4$^+$ T cells.

(B) Gating strategy for Tregs in heterozygous females to distinguish mutant Treg (Thy1.1$^-$Foxp3$^+$) from WT Treg (Thy1.1$^+$Foxp3$^+$).

(C) Foxp3 staining in splenic mutant Tregs, gated as in (B), in heterozygous females, and its quantification in a dot plot. MFI quantification at right was normalized vs. the mean MFI of WT littermates from the same experiment and background (B6 or B6.*Foxp3-ires-gfp*). Each dot is an individual mouse.

(D) Foxp3 mRNA expression in mutant Tregs, from RNA-seq profiling, also normalized to the mean of matched WT controls. Each dot is an individual mouse.

(E) DNA-binding capacity of the different mutations in HEK293T cells. HA-tagged FOXP3 molecules (WT or mutant) were transiently expressed in 293T cells, pulled down by anti-HA beads, and incubated with FOXP3-binding ds-oligonucleotide IR-FKHM4g.[33] Left: representative blot; right: quantitation from 3 independent experiments; t test *$p < 0.05$, **$p < 0.01$.

effects, we studied heterozygous females, which are protected from inflammation by the presence of WT Tregs,[1,3,20] mutant Tregs competing with normal Tregs driven by the WT *Foxp3-Thy1.1* allele (Figures 1B and S1C; for clarity, the presentation below only refers to Thy1.1-negative mutant Tregs). All lines, except for R337Q, had normal proportions of Tregs expressing

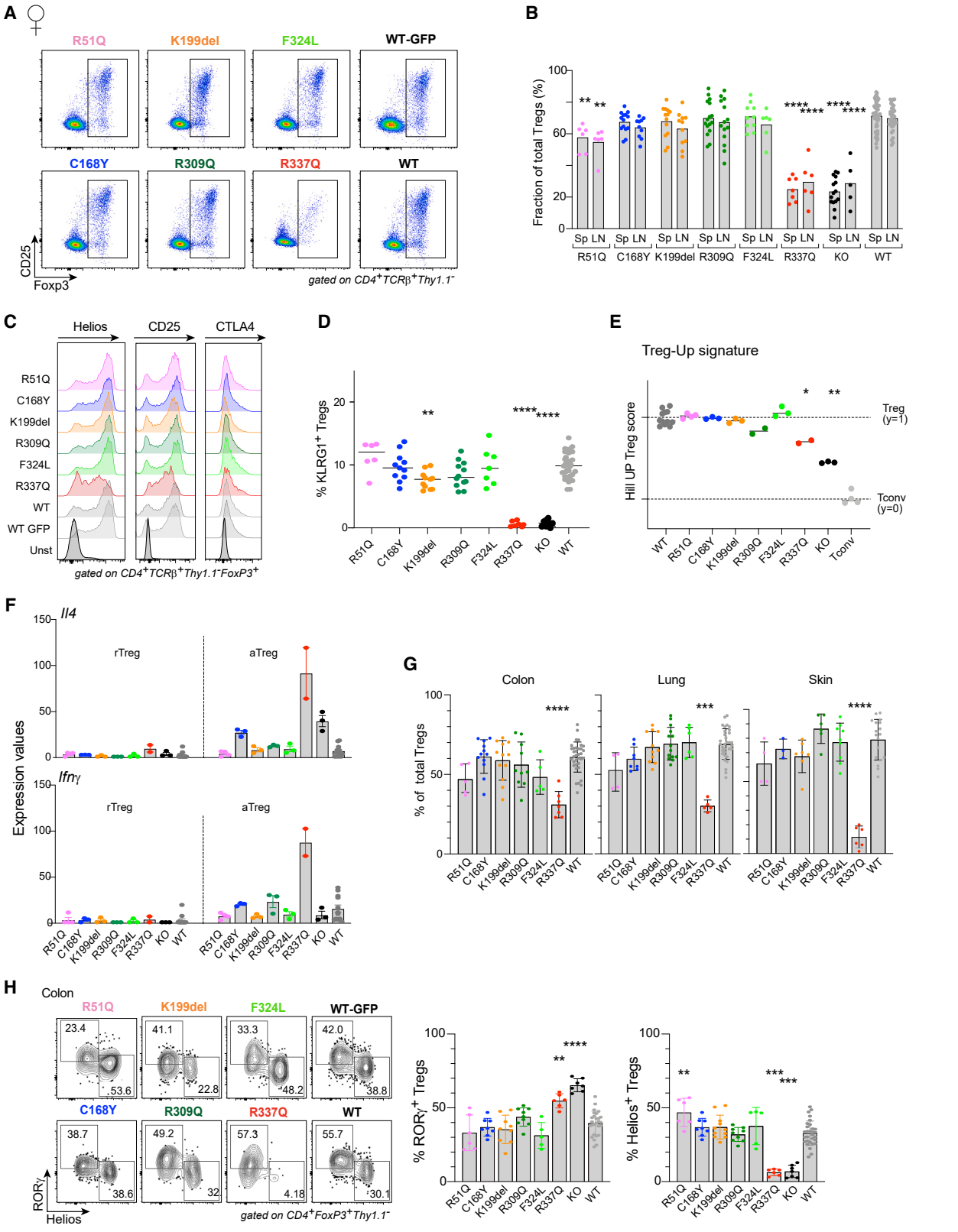

(legend on next page)

the mutant FoxP3 proteins in lymphoid organs, as shown by Foxp3/CD25 plots (Figures 2A and 2B). The R337Q mutation induced a significant decrease in mutant Treg proportions to a level similar to that of the full KO (Figure 2B), accompanied by a drop in FoxP3 and CD25 mean fluorescence intensity (MFI). K199del Tregs also showed reductions in FoxP3 and CD25, but these were more muted (Figures 2A and 2C).

We then analyzed more broadly Treg phenotypes in FoxP3 mutant mice. Except for R337Q, typical Treg markers like Helios, CD25, and CTLA-4 were normally expressed in Tregs from all mice (Figure 2C). Tregs in lymphoid organs exhibit significant diversity but are most simply grouped as "effector" or "activated" (aTreg) and "resting" (rTreg) Treg populations. Since aTregs have higher anti-inflammatory potential,[38–40] we asked if the mutations impacted the ability to mature into aTregs. Screening a panel of effector markers showed that the mutations did not impair aTreg maturation or *in vivo* proliferative capacity reflected by Ki67. However, R337Q (and, more subtly, K199del) led to the total absence of the KLRG1$^+$ Treg subset and to a significant decrease in CD44^{hi}CD62^{lo} Tregs (Figures S2A, S2B, and 2D).

A possible loss of Treg identity was investigated by RNA sequencing (RNA-seq) profiling of purified CD4$^+$TCRb$^+$CD25^{hi} Thy1.1$^-$ Tregs, profiling separately the CD44$^-$CD62L^{hi} (rTreg) and CD44^{hi}CD62L$^{lo/-}$ (aTreg) populations (normal Foxp3-Thy1.1$^+$ Tregs from some of the same mice were also profiled and showed no deviation). With a "Treg score" calculated from canonical "Treg signature" transcripts,[7] these FoxP3$^+$ cells were indeed *bona fide* Tregs, with a strong bias for expression of Treg signature genes (Figure 2E). R337Q was the exception, with a score intermediate between normal and FoxP3-deficient Treg "wannabes" in full KO mice.[3,8,10,41] Normal expression of the Treg signature was confirmed on volcano plots (Figure S2C) and ranked signature plots (Figure S2D), which highlighted the marked shift in R337Q Tregs but also uncovered deviations in signature genes in some mutant Tregs (R51Q, K199del, R309Q), further detailed below. An essential FoxP3 function is cytokine-encoding gene repression, like *Ifng*. Among mutants, derepression of cytokine genes was evident for R337Q Tregs, as illustrated for *Ifng* and *Il4* (Figure 2F); other mutant lines closely mirrored WT controls (with perhaps the exception of *Il4* in C168Y).

To finish this survey of Treg populations, we verified their ability to migrate and reside in non-lymphoid tissues (Figure 2G). Mutant Tregs were found in similar proportions as WT Tregs in the colon, lung, and skin (Figure 2G), again with the exception of R337Q. R337Q Tregs were outcompeted to different degrees, especially in the skin (Figure 2G). Colonic Tregs include a balance of Helios$^+$ and RORg$^+$ subsets.[42] Only R337Q perturbed this ratio, with a dramatic dearth of Helios$^+$ colonic Tregs (Figure 2H), which is of interest in light of recent reports that Helios$^+$ Tregs are far more dependent on FoxP3 than RORg$^+$ Tregs.[20,43]

Overall, most of these IPEX-causing mutations allowed quasi-normal Treg differentiation and homeostasis in heterozygous females, with R337Q being the notable exception.

Impact of the missense mutation in hemizygous males

We then studied the effects of FoxP3 mutations in hemizygous males, a context similar to that of IPEX patients, without the protection from WT Tregs found in heterozygous females. At 8 weeks old, these mice were devoid of overt signs of pathology. Tregs were present in lymphoid organs of mutant mice in the same proportion as in WT males, except for R337Q, which showed a 2-fold increase, the opposite of the change noted in females (Figures 3A and 3B). R337Q Tregs also recovered FoxP3 and CD25 expression to levels closer to those of WT Tregs (Figure S3A); R337Q mice also included a sizable proportion of FoxP3^{int}CD25$^-$ cells, as was already described in full FoxP3 deficiencies[3,8,10,41] (Figure 3A). In contrast, the mild decrease in FoxP3 MFI noted in K199del females was also present in males (Figures 3A and S3A). R337Q Tregs were characterized by a high activation state (Figures 3C and S3B)—although less than in the full KO—and upregulated various aTreg markers like PD-1, KLRG1, and CXCR6 (Figures 3D and S3B). In non-lymphoid tissues, mutant males had normal Treg proportions, except for R337Q, which had an increase in gut, lungs, and skin (Figure 3E), a mirror image of the paucity of tissue Tregs observed in R337Q females. Finally, and perhaps most striking, was the subset distribution among colonic Tregs of R337Q males: a high proportion of Helios$^+$ Tregs and fewer RORg$^+$ Tregs (Figure 3F)—again, the exact opposite of the ratio observed in females (Figure 2G).

In short, most mutations had little impact on Treg homeostasis at baseline in hemizygous males, except for R337Q. The contrast in cell phenotypes between males and females highlighted how the interaction between intrinsic Treg dysfunction and the cellular environment (including competition from WT Tregs) can influence the expression and impact of the mutations.

Pathological effects of missense mutations

The next step was to investigate the mutation's impact on immunological tolerance in hemizygous males. We first explored it in

Figure 2. Treg phenotypes in heterozygous females

(A) Representative flow cytometric CD25/FoxP3 plots of gated CD4$^+$TCRB$^+$Thy1.1$^-$ splenocytes from heterozygous females; the two WT littermates shown are from the B6 and B6.*Foxp3-ires-gfp* backgrounds.

(B) Proportions of Tregs expressing the mutant FoxP3 among total Tregs in spleen from heterozygous females.

(C) Expression of Helios, CD25, and CTLA-4 in FoxP3$^+$ Tregs (representative of at least 3 experiments).

(D) Proportions of KLRG1$^+$ cells among splenic Tregs from heterozygous females.

(E) rTregs were sorted as CD19$^-$TCRB$^+$CD4$^+$CD25$^+$Thy1.1$^-$ and their RNA-seq profiles determined. The Treg-Up gene expression signature from Hill et al.[7] was used to compute a Treg score (scaled to WT Treg = 1 and Tconv = 0).

(F) Expression of *Il4* and *Ifng* transcripts in Tregs in the RNA-seq data from (E).

(G) Proportions of Tregs expressing the mutant FoxP3 among total Tregs in different tissues.

(H) Representative RORg/Helios plots of colon Tregs expressing the different mutant FoxP3 or WT control littermates (quantification of multiple experiments at bottom).

All results are from 2–4 independent experiments; each dot is an individual mice; error bars indicate mean ± SD; *p < 0.05, **p < 0.01, ***p < 0.0001, ****p < 0.0001, from Mann-Whitney test.

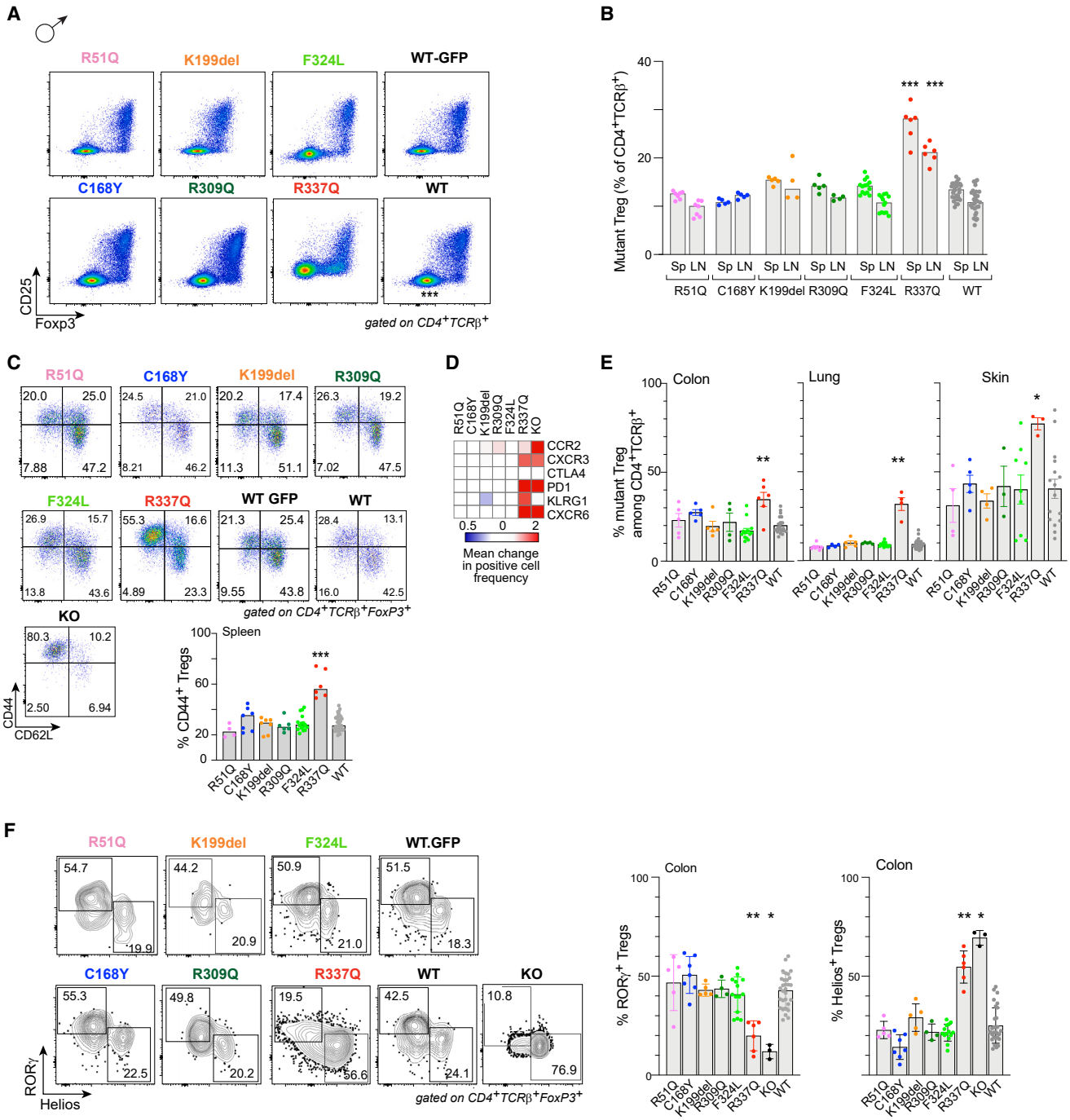

Figure 3. Treg phenotypes in hemizygous males

(A) Representative CD25/FoxP3 plots of gated CD4$^+$TCRB$^+$Thy1.1$^-$ T splenocytes from hemizygous males; the two WT littermates shown are from B6 and B6.*Foxp3-ires-gfp* backgrounds.

(B) Proportions of Tregs expressing the mutant FoxP3 among CD4$^+$TCRβ$^+$ cells in spleen from hemizygous males.

(C) Representative CD44/CD62L plots of splenic Tregs from the different mutants and two WT control littermates (quantified at bottom).

(D) Cumulative heatmap of the change in proportion of different markers in the splenic Treg from the mutants, each normalized to its WT littermate.

(E) Proportions of Tregs expressing the mutant FoxP3 in different tissues.

(F) Representative RORg/Helios plots of colonic Tregs expressing the different mutant FoxP3s or from WT control littermates (quantification from multiple experiments at right).

All results are from 2–3 independent experiments; each dot is an individual mouse; error bars indicate mean ± SD; *p < 0.05, **p < 0.01, ***p < 0.0001, from Mann-Whitney test.

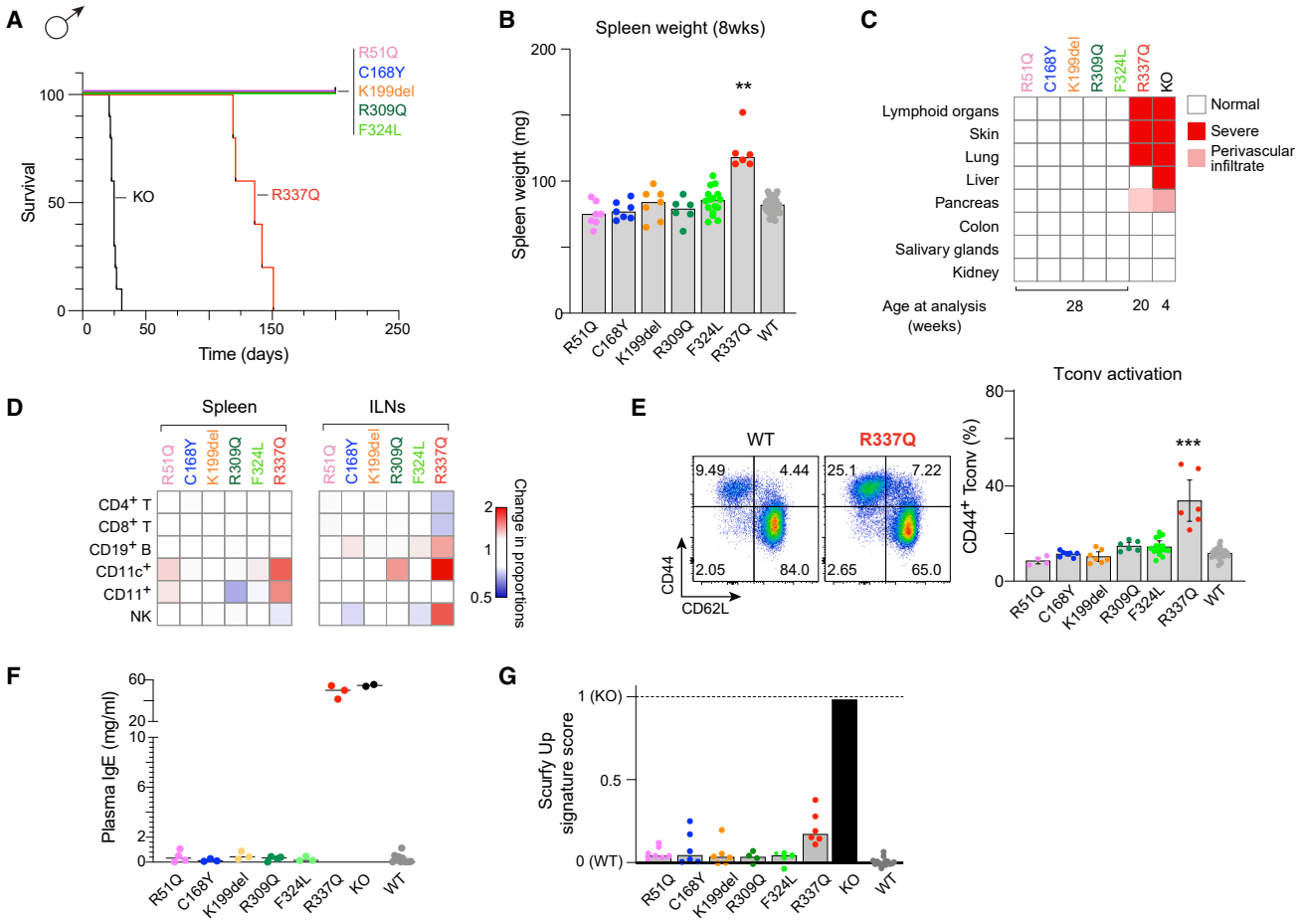

Figure 4. Autoimmune disease manifestations in hemizygous mutant males at baseline

(A) Survival curve of mutant males.

(B) Spleen weight at 8 weeks of age.

(C) Representative heatmap of the pathological changes in male mutants, at 28 weeks of age for all mice except KO (4 weeks) and R337Q (20 weeks).

(D) Heatmap of averaged changes in immunocyte proportions in spleen and inguinal lymph nodes (ILNs) for each mutant line relative to its WT littermates.

(E) Representative flow cytometry CD44/CD62L plots from R337Q and WT littermate Tregs. (quantification from multiple experiments at right).

(F) Plasma IgE concentration, quantified by ELISA.

(G) Scurfy-Up transcriptomic score among resting splenic Tregs (scaled from WT Treg = 0 and *FoxP3* KO Treg = 1).

unchallenged mice. None of the mutant mice showed the rapidly lethal wasting disease of mice with full FoxP3 deficiency (Figure 4A), and most lines thrived during a 6 month follow-up (Figure S4A). However, R337Q began to develop skin lesions around 10–12 weeks of age, associated with growth stagnation, leading to death around 22 weeks of age (Figures 4A and S4A). Lymphoproliferation was already present at 8 weeks in R337Q males with a splenomegaly and diffuse adenopathies (Figure 4B) and was far more pronounced at 20 weeks (Figure S4B). In older mice, while severe leukocyte infiltrates were found in the skin and lungs of R337Q mice, but not in the liver (Figures 4C and S4C), all the other mutants were free of inflammation in all parenchymal tissues screened (skin, lungs, colon, liver, pancreas, kidney, salivary gland; Figure 4C).

Dysregulation of other immunocyte populations is a hallmark of Treg dysfunction.[44] We thus examined other cell types in lymphoid organs in these mice. Only R337Q showed changes: proportions of dendritic, myeloid, and natural killer (NK) cells were increased in the spleen and lymph nodes (LNs) (Figure 4D), along with a stronger activation of Tconvs (Figure 4E). Additionally, R337Q showed elevated plasma immunoglobulin E (IgE) levels (Figure 4F), as has been described in most patients with IPEX and in Treg-deficient mice[5,30,32,45–47] (Figure 4F). Accordingly, high frequencies of IL-4-producing cells were observed in R337Q and KO mice (Figure S4D).

In FOXP3-deficient males (human or mouse), a characteristic "IPEX signature" or "scurfy signature" is present in the transcriptome of all CD4+ T cells and Tconvs as well as Treg-like cells, which reflects the immunologic dysregulation and/or the homeostatic drive that attempts to restore Treg function.[3] As another measure of disease, we generated RNA-seq profiles from Treg-like cells in mutant males, and a biased expression of this signature was observed in R337Q Tregs, albeit not as marked as in KO Tregs, but not for any of the other missense mutations

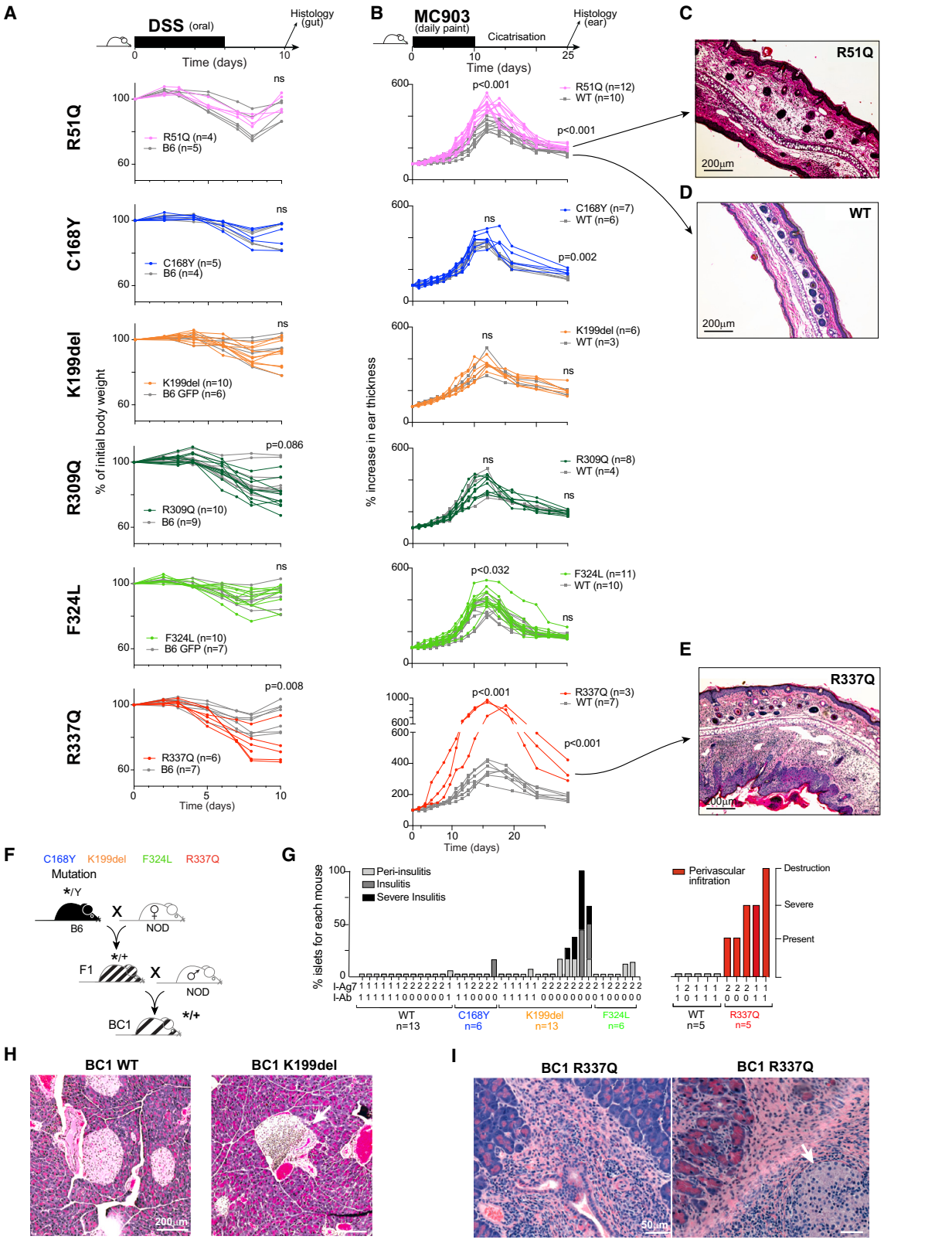

(legend on next page)

(Figures 4G and S4E). This bias was concordant with the overall pathology of the mutants.

Pathology revealed by immunologic challenges

We continued to be surprised by the paucity of effects resulting from these mutations, with the exception of R337Q, even though they had been identified in patients with IPEX with clear disease. Tregs in these mice appeared in normal numbers and of normal phenotypes and maintained self-tolerance at baseline. This discrepancy could be due to environmental triggers and/or genetic cofactors revealing Treg dysfunction in patients with IPEX given the variability seen in patients bearing the same *FOXP3* mutation. Accordingly, we exposed 8-week-old mutant males to various challenges related to the IPEX pathological triad, enteropathy with dextran sodium sulfate (DSS) colitis,[48] eczema with the MC903 model of atopic dermatitis,[49] and type 1 diabetes (T1D), by introducing susceptibility variants from diabetes-prone NOD/ShyLtJ mice,[50,51] all being models known to be affected by Tregs.

DSS colitis induces a strong Treg response, and its course is impacted by Treg fitness.[52,53] We followed the standard protocol (6 day DSS treatment, 4 day recovery; Figure 5A). R337Q males exhibited a stronger response and retained pathology at day 10. Other mutants responded as the controls, except for an inconstant trend in R309Q.

Second, we induced atopic dermatitis-like lesions in the ears with topical MC903, a vitamin D analog.[49] R51Q males showed significantly increased responses, a stronger acute phase, and persistent inflammation (Figure 5B), with residual ulceration and acanthosis in the ears at day 25 (Figure 5C). Control littermates were essentially clear of sequalae (Figure 5D). As in the DSS model, responses to MC903 were explosive in R337Q males (Figure 5B), with uncleared inflammation 2 weeks later (Figure 5E). None of the mutant ears displayed fibrosis at day 25 (Figures 5C–5E and S5).

Diabetes in NOD mice is controlled dominantly by alleles of major histocompatibility complex (MHC) class II molecules (H2-A^{g7}) and by a collection of other loci that collectively contribute to dysfunctional tolerance.[51] NOD males are also far less susceptible to T1D than females. We reasoned that focal defects in FoxP3 and Treg function might be revealed in the context of a partial complement of NOD susceptibility alleles that would be insufficient alone to engender autoimmune diabetes. Males from intercrosses or first-generation backcrosses between non-susceptible inbred strains (like our B6 mutants) and the NOD strain never present with diabetes, and show only sporadic and tardy insulitis,[54,55] because genetic susceptibility alleles needs several generations to be established. Thus, we bred first-generation backcross (BC1) mice onto NOD from four mutant lines (Figure 5F), monitoring these BC1 for diabetes and scoring insulitis at 18–20 weeks of age. No overt diabetes was observed except in one of the R337Q BC1 mice. Clear peri-insulitis and insulitis, which resembled insulitis in NOD mice but spread to many islets, was observed in K199del BC1s (Figures 5G and 5H) but not in the other mutant or control mice. Insulitis in these mice was "respectful"[56] in that it coexisted with healthy-looking beta cells in the same islets (Figure 5H). Importantly, no insulitis was observed in K199del BC1 mice that carried one copy of the B6-derived H2-Ab allele, which is normally protective,[57] indicating that autoimmunity in K199del males was still under MHC control. Backcrossed R337Q mice showed a very different phenotype: there was no insulitis, but perivascular/ductal spaces showed extensive vasculitis that damaged exocrine tissue (Figures 5G and 5I; with complete destruction in some cases) but respected the islets (Figure 5I, right panel). This peri-vascular infiltrate was similar to pancreatic infiltration observed in full *Foxp3* KO mice and was independent of MHC control, as it occurred equally in $A^{g7/g7}$ and $A^{g7/b}$ mice (Figure 5G).

Thus, challenging the immune system revealed covert susceptibilities in FoxP3 mutant mice. This susceptibility was revealed in different locations as a function of the particular mutation (skin for R51Q, islets for K199del), the latter influenced by the MHC and autoimmune susceptibility genes, unlike the *scurfy*-like pancreatic vasculitis of R337Q mice.

Mutation-associated transcriptional changes

Given the range and specificity of phenotypes resulting from the different FoxP3 mutations, we sought to identify transcriptional modules specifically affected by these mutations that would give us clues about underlying mechanisms of pathogenesis. We analyzed heterozygous females in order to determine the intrinsic effects of each mutation and purified separately rTregs and aTregs for population RNA-seq to differentially analyze the impact of FoxP3 in the two states (Figure 6A). Each mutation was analyzed (in 2–4 biological replicates) in comparison with sex- and background-matched WT littermates.

Most of the mutations induced very few transcriptomic changes relative to WT Tregs, with 15–77 differential transcripts

Figure 5. Genetic or inflammatory challenges reveal hidden phenotypes in FoxP3 mutant males

(A) Induced colitis: weight loss in DSS-treated mutant males and their control littermates.

(B) Induced dermatitis: ear thickness in MC903-treated mutant males and their control littermates.

(C–E) Representative images of H&E staining of ear sections from MC903-treated mice at the resolution phase of dermatitis (day 25): R51Q (C), WT (D), and R337Q (E).

(F) Breeding of first backcross (BC1) onto the NOD background.

(G) Pancreatic autoimmunity. Left: insulitis score in hemizygous BC1 male pancreata of the 3 mutant lines shown (0: normal; 1: peri-insulitis; 2; insulitis; 3: severe insulitis); each bar is an individual mouse (>15 islets scored/mouse), with WT littermates of the three lines combined for simplicity. Right: scoring of perivascular infiltrates in R337Q BC1 pancreata (present: several perivascular infiltrates, intact exocrine acini; severe: abundant perivascular infiltrates, with destruction of surrounding acini in some regions, intact islets; destruction: quasi-complete destruction of the exocrine pancreas).

(H) Representative severe insulitis (arrow) in a K199del BC1 pancreas and normal islet from a WT pancreas.

(I) Representative perivascular infiltrates R337Q BC1 pancreata; note how the severe inflammation at right dilacerates the acinar tissue but leaves the islet (arrow) comparatively intact.

All results are from hemizygous males and from 2–5 independent experiments; p values from Mann-Whitney test.

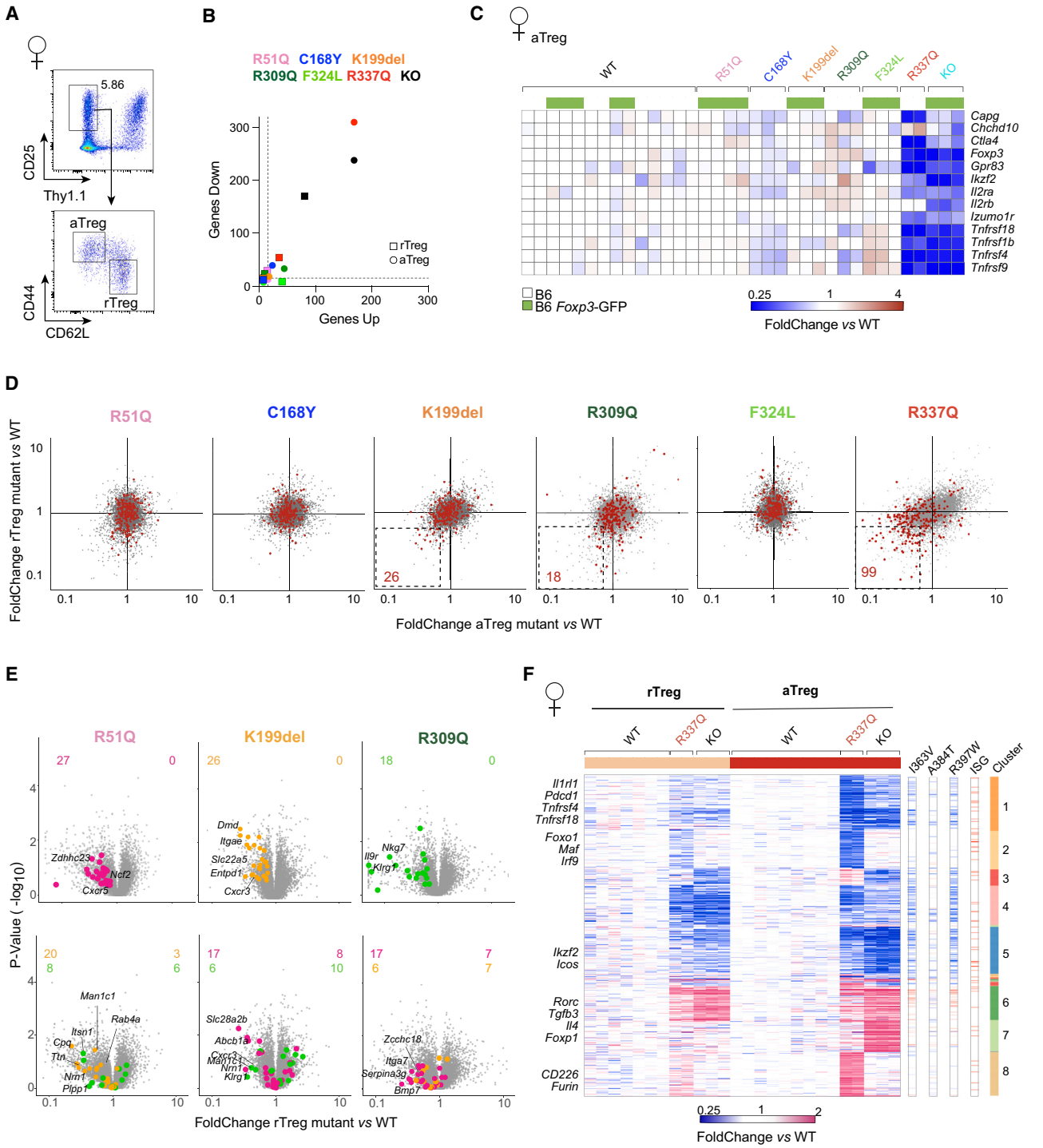

Figure 6. Transcriptional changes resulting from the mutations

Low-input RNA-seq was performed on Tregs expressing the FoxP3 mutants in heterozygous females and matching WT littermates.

(A) Representative gating to isolate Treg (Thy1.1-CD25^{high}) from mutant or WT littermates. Bottom: gating of rTreg and aTreg subsets.

(B) Numbers of differential expressed genes (at arbitrary thresholds of fold change <0.5 or >2, and t test $p < 0.01$) in aTreg (round) or rTreg (square) in the various mutants vs. averaged values from their matched WT littermates. Experimental noise in these datasets was estimated by recomputing apparent differentially expressed genes (DEGs) after permuting the data labels.

(C) Heatmap of the mutant/WT fold change, for core Treg genes (defined in Zemmour et al.[35]), calculated for each donor mouse against the averaged expression in all WT Tregs from matching backgrounds (B6 or B6.*Foxp3-ires-gfp*) (indicated on top); each column is an independent mouse.

(legend continued on next page)

(at arbitrary thresholds of 2-fold and t test nominal $p < 0.01$; Figure 6B; corresponding volcano plots are shown in Figure S6A). These values were not much higher than the noise estimated by permutation analysis (Figure 6B). The exception was R337Q, with 578 differentially expressed genes in the aTreg dataset. Lists of FoxP3-dependent genes have been defined, mostly from comparative profiling of Tregs in heterozygous FoxP3-deficient females,[3,19,20] including a narrow "core Treg signature" of genes that appear to be intrinsic targets of FoxP3.[3,35] There was very limited impact for R51Q, C168Y, K199del, R309Q, and F324L on these core Treg transcripts (Figure 6C), while R337Q aTregs showed an almost total downregulation, with the exception of *Chchd10* and *Il2rb*, both of which were well downregulated in the KO control (Figure 6C).

These results denoted a very narrow and mild imprint of most of the Foxp3 mutations. Thus, we plotted together the changes observed in rTregs and aTregs, reasoning that concordance in both datasets would increase the reliability and power to detect subtle effects. We also focused on an external list of *Foxp3*-dependent genes[20] (Figure 6D). As a proof of principle, most downregulations in R337Q Tregs were clearly present in both Treg states, albeit with quantitative differences (Figure 6D, right). K199del and R309Q showed a few genes with reproducible downregulation, although the FoxP3-dependent signature as a whole was not significantly shifted. No trend was noted for C168Y and F324L, while R51Q induced a downregulation of part of the signature, mostly in rTregs. To substantiate the latter, we generated data from other R51Q mice that derived from an independent founder line, which confirmed this subtle downregulation in R51Q rTregs (Figure S6B). No such signal was found in aTregs of either R51Q line. We then asked if these subtle changes in R51Q ($n = 27$), K199del ($n = 26$), and R309Q ($n = 18$) were specific for each of the N-terminal mutations or were shared between the three non-FKHD mutations (Figure 6E; Table S3). There was some sharing of the genes affected by the N-terminal mutations R51Q and K199del, whereas R309Q had its own footprint. As expected given the small number of genes affected, Gene Ontology and pathway analysis did not reveal any significant enrichment, nor could we find clues explaining the phenotypic specificity. There was also no significant overlap with the changes observed in the gene expression profiles from the original patients with IPEX (not unexpected given the weak changes in mice and $n = 1$ patient). We also searched genome-wide association study (GWAS) databases for loci implicated in human autoimmune diseases. Although not a statistically significant overlap, two of the reproducible targets revealed in the R51Q mutant (*NCF2* and *ZDHHC23*) had been associated with autoimmune diseases with strong skin manifestations, systemic lupus erythematosus, and psoriasis, respectively (Table S3).

As evidenced in Figure 6C, the impact of R337Q on Treg core signature genes was similar but not identical to that of a complete FoxP3 LOF. Broader investigation (Figures 6F and S6C) showed that many of the changes seen in Treg-like "wannabes" from KO females were also present in R337Q Tregs, albeit milder (e.g., clusters 5, 6, and 7 in Figure 6F). In addition, two gene clusters were uniquely induced or repressed in R337Q but not in KO aTregs (clusters 2 and 8 in Figure 6F; Table S4). To further assess the specificity of these R337Q effects, we retrieved gene expression profiles from previous studies of FKHD mutations in mice.[30] The R337Q-specific clusters were not observed with these mutations either (Figure 6F, right), nor with other mutations in our present panel (Figure S6D). Interferon-response pathway and nuclear factor κB (NF-κB) signaling genes were specifically enriched in cluster 2. The R337Q mutation hinders the recently discovered head-to-head dimerization of FoxP3,[33] and we speculate that the consequences of R337Q that are not shared with complete FoxP3 LOF or other FKHD mutants may stem from its ability to form some, but not other, DNA-binding conformations.

Finally, we compared the effect of the mutations at 8 weeks of age in female and male Tregs (the latter without competition from WT Tregs but in a partially destabilizing milieu). We focused on R337Q since the consequences of the other mutations were too subtle to validly allow such a comparison. In rTegs, the effects were very similar (Figure S6E), but in aTregs, the comparison proved more complex: some transcripts were equally affected in both contexts, but many were affected only in heterozygous female aTregs. These disparities likely underlie the paradoxically opposite phenotypes of R337Q-expresssing Tregs in hemizygous males and heterozygous females noted in Figures 2 and 3.

Effects of FoxP3 mutations at the chromatin level

The mutant mouse lines thus seemed to identify two classes of mutations from patients with IPEX. R337Q yielded a "*scurfy*-like" phenotype, with transcriptional changes and immunological manifestations that resemble those of full LOF or mutations that strongly interfere with DNA binding[29,30,32,58] and others, exemplified by R51Q or K199del, whose transcriptional consequences were more discrete, were mostly distinct, and led to focused Treg defects different from those of scurfy disease. Because chromatin structure can yield a more robust landscape of gene regulatory programs than RNA-seq (i.e., not affected by transcriptional bursting, mRNA stability), we performed single-cell assay for transposase-accessible chromatin sequencing (scATAC-seq) on purified Tregs (Figures S7A and S7B). We focused on three mutants that exemplified these classes, sorting splenic Tregs from heterozygous females (and their corresponding WT littermates)

(D) Comparison of mutant/WT fold changes in aTreg (x axis) versus rTreg (y axis), for each mutant, highlighted with FoxP3-dependent genes (genes downregulated in the absence of FoxP3 in van der Veeken et al.[20]).
(E) Fold change vs. p value plots comparing normalized expression in mutant Tregs from heterozygous females with WT Tregs from the same background (B6 or B6.*Foxp3-ires-gfp*). Highlights correspond to the "concordant" FoxP3-dependent genes between rTreg and aTreg comparisons (for K199del or R309Q, defined in D) or between the two independent founder lines for R51Q (per Figure S6B).
(F) Heatmap of transcripts differentially expressed in R337Q and KO relative to matched littermates (selected on arbitrary threshold as in A) shown is expression is normalized to the mean of matched control littermates; each column is an independent mouse. Overlap with DEGs described in previous FoxP3 mutations,[30] and interferon-sensitive genes are shown at right.

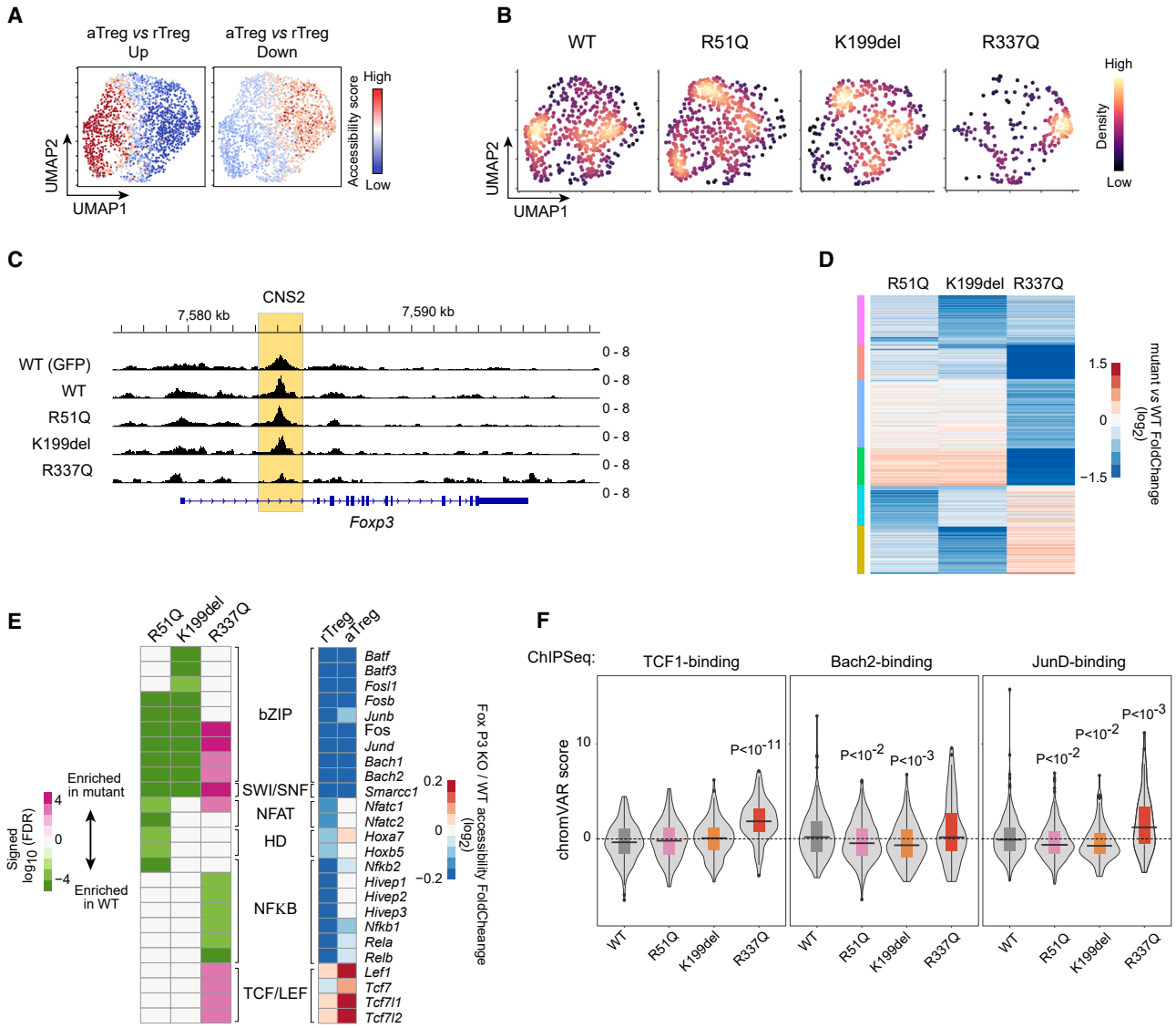

Figure 7. Changes in chromatin architecture in Tregs from heterozygous mutant females

Single-cell ATAC-seq was performed in multiplex mode on Tregs from heterozygous mutant females and their WT littermates.

(A) UMAP representation of the ATAC signal, grouping cells from all mice. The relative accessibility (chromVAR scores) in each cell was computed for OCRs that distinguish aTreg and rTreg populations.

(B) Density of Tregs from WT and FoxP3 mutant mice, overlaid onto the same UMAP as in (A).

(C) Aggregated accessibility profiles at the *Foxp3* locus for Tregs expressing the mutant or WT FoxP3; *Foxp3* CNS2 region is highlighted.

(D) Differential accessibility: heatmap of mutant/WT fold change (log2) in aggregated chromatin accessibility of Tregs from each mutant vs. its respective WT littermate (ordered by k-means).

(E) TF involvement: TF binding motifs enriched (at FDR < 1×10^{-3}) in OCRs differentially accessible in mutant vs. WT aTregs (pink and green, enriched in mutant or WT, respectively). Right: for reference, the log2 fold change in accessibility KO Tregs vs. WT for OCRs that contain the corresponding TF motifs (data from Chowdhary et al.[43]), split between rTregs and aTregs.

(F) Distributions of per-cell relative accessibility (chromVAR score) of OCRs within genomic regions that bind TCF1, Bach2, or JunD determined by ChIP-seq (data from van der Veeken et al.[20] and Grant et al.[63]) among aTregs from each genotype. Nominal t test p values.

and hash tagging cells from all genotypes in the same run[59] for optimal comparability. Relative accessibility (chromVAR score[60]) of open chromatin regions (OCRs) that characterize Treg states[43] readily distinguished aTregs and rTregs on a 2D uniform manifold approximation and projection (UMAP) visualization of the combined data (Figure 7A). Tregs from each genotype occupied distinct regions of the UMAP space (Figure 7B). Whereas R51Q and K199del mutant cells largely comingled with WT cells, albeit with different preferential densities, R337Q Tregs shifted away from other WT and mutant cells (Figures 7B and S7C). Most of these R337Q cells were in a resting-like chromatin state, consistent with the flow cytometry (Figure S2). This dichotomy was

also observed at the *Foxp3* locus itself. While K199 and R51Q Tregs showed no notable alterations, R337Q Tregs had decreased accessibility at CNS2, a *cis*-regulatory element bound by FoxP3 itself, locking in the stability of *Foxp3* expression[61,62] (Figure 7C). We confirmed this change in accessibility at CNS2 by bulk ATAC-seq (Figure S7D). Thus, R337Q, but not the N-terminal mutations R51Q and K199del, impaired epigenetic feedback that controls *Foxp3* expression. The differences in these two classes of mutants extended to a global level: a small subset of differential OCRs showed consistently decreased accessibility across all mutants, but OCRs with increased accessibility in R337Q cells had opposite effects in K199 and R51Q cells, and vice versa (Figure 7D).

FoxP3 collaborates with other TFs via direct protein-protein interaction and colocalization at regulatory regions.[18,64,65] How did each FoxP3 mutation affect the activity of other TFs? To address this question, we searched for TF binding motifs enriched (at FDR $<1 \times 10^{-3}$) in OCRs differentially accessible in mutant vs. WT Tregs. To avoid confounding effects resulting from changes in cell population abundance, we stratified comparisons between WT and mutant cells by cell state (rTregs or aTregs, per Figure 7A). The results portrayed very different effects of the mutations (Figure 7E, left). A number of OCRs were more accessible in R337Q mutant aTregs relative to WT aTregs. These were enriched in motifs that bind key Treg regulators, including those of the TCF/LEF and bZIP families, while OCRs with decreased accessibility in R337Q relative to WT aTregs were enriched for NF-κB motifs (Figure 7E, left panel; for reference, the average change in accessibility of OCRs that contain these motifs in fully FoxP3-deficient Tregs[43] are shown at right). In contrast, OCRs whose accessibility was reduced by R51Q and K199del mutations were enriched in a distinct set of motifs, partially overlapping between the two (in particular, bZIP-binding motifs for Bach or Fos and also NF-AT motifs). There were very few changes among rTregs, with only increased TCF/LEF motif enrichment among R337Q mutants, consistent with the aTreg effects. While TCF/LEF motif-containing sites increased in accessibility in both the R337Q mutant and full KO, bZIP motif-containing sites increased in accessibility among R337Q Tregs but had diminished accessibility in the full KO (Figure 7E). While only a subset of full KO changes was present in the non-FKHD R51Q and K199del mutations, those that were present were consistent with the direction of effect elicited by complete FoxP3 deficiency (Figure 7E). To orthogonally validate these findings using *bona fide* TF binding data, we examined the per-cell relative accessibility (chromVAR score) of OCRs known to bind TCF1, Bach2, and JunD from independent chromatin immunoprecipitation (ChIP)-seq data[20,63] and containing the corresponding motifs. Consistent with the motif-enrichment results, R337Q Tregs showed increased accessibility at JunD- and TCF1-bound sites; the latter likely corresponded to increased expression of its mRNA (Figure S7E). These effects are consistent with the notion that FoxP3 represses TCF-1 expression, accounting for the indirect part of its action.[20] On the other hand, R51Q and K199del cells had decreased accessibility at Bach2- and JunD-bound sites (Figure 7F). Thus, the divergence between mutations inside vs. outside the FKHD extended to global differences in the activities of FoxP3 partner TFs.

DISCUSSION

This porting of mutations from patients with IPEX into mice, allowing comparative analyses in robust numbers (beyond N = 1 in patients) and with control of genetic and immunologic variables, uncovered an unexpectedly multifaceted aspect of IPEX-causing *FOXP3* mutations and thus of FoxP3 function. It exposed the distinction between two classes of IPEX-causing mutations, that different mutations elicited preferential effects on chromatin that involved different sets of cofactors, and that immunologic or genetic perturbations were necessary to manifest the specific disease facets tied to each mutation. The comparison of Treg-like cells that express the same mutant FoxP3 protein in mutant males and carrier females also showed that the behavior varied strikingly as a function of the organismal environment, emphasizing the importance of cell-extrinsic regulatory loops in modulating Treg function.

This panel distinguishes two classes of *FOXP3* mutations in which we can also integrate the isolated mutations analyzed previously by others and ourselves. In the first class, the FKHD mutant R337Q echoed strongly the phenotypes already described in various missense FKHD mutations in mice (A384T, M370I).[30,32] Their phenotypes appeared like a "slowed-down" version of the full *scurfy* LOF phenotype: a number of manifestations appeared in unperturbed mice, including skin and lung inflammation, activation of many immunocytes, and dysregulated IgE levels. The R337Q mutation also reproduced most of the transcriptional alterations of full LOF cells (albeit in a muted fashion), with a reshuffling of the Treg chromatin architecture, the loss of repression by TCF1, and diminished positive feedback by FoxP3 at the CNS2 element of the *Foxp3* locus. Although the genomic studies were not as extensive in previous studies, many of the phenotypic traits were the same as those previously reported in mice with partial LOF mutations in the FKHD (A384T, M370I[30,32]), in particular the hyper-IgE and IL-4 over-expression, which we had also noted *in vitro* with strong FKHD mutations.[18] The second class encompasses mutations in other domains of FoxP3, i.e., are not involved in DNA binding (at least not as directly). These mutations preserved the general distribution of chromatin architecture across Treg diversity, maintained the ability of FoxP3 to repress TCF-1 and LEF1, and only induced very subtle transcriptional changes; affected males showed essentially no alterations in baseline immunoregulation, with no Th2 deviation or hyper-IgE production. The chromatin accessibility data suggest that mutations of the second class impacted FoxP3-controlled chromatin regions that involved a different segment of the cofactors that partake in the Treg regulatory network. For instance, they diminished accessibility at Bach2- and JunD-binding sites, which were actually boosted by the R337Q mutation. This dichotomy concords with results from clinical studies, in which, generally speaking, FKHD mutations are generally more severe.

Importantly, the full physiological importance and specificity of these mutations was revealed only by additional perturbations: inflammatory for R51Q and R309Q (and R337Q) and genetic for K199del. These observations bolster the hypothesis that the heterogeneity of onset age and clinical phenotypes displayed by patients bearing the same mutation results from

genetic or immunologic covariates.[26,66–68] In these contexts, the facets of autoimmune dysfunction also differed according to the mutation: exacerbation of autoimmune diabetes for K199del or of skin inflammation for R51Q. This diversity, which contrasts with the more monomorphic consequences of FKHD mutations, evokes the phenotype of a mouse with a GFP fusion into the N terminus of FoxP3, which protected from arthritis but accelerated autoimmune diabetes.[69,70] Mechanistically, insertion of the bulky GFP domain disrupted a number of interactions by FoxP3 (TIP-60, Ikzf4, HIF-1α, Irf4), thus causing the bias Treg function.[69,70] In the same vein, we suggest that the R51Q and K199del mutations affect particular interactions in which FoxP3 engages, and those conditioned the differential Treg dysfunction in the present mice. It is interesting that the transcriptional consequences of R51Q were most marked in rTregs, while those of K199del were equally seen in rTegs and aTregs. Unfortunately, the transcriptional differences between R51Q- and K199del-expressing Tregs proved too subtle to rigorously nominate the candidate transcripts and functions that underpin these outcomes.

The diametrically opposed phenotypes of Tregs expressing R337Q in male and female settings were quite striking. This outcome very likely reflected the balance of cell-extrinsic and -intrinsic consequences of the mutations observed in cells from patients with IPEX and their heterozygous female relatives,[3] and in earlier observations in FoxP3-deficient mice,[3,41] but the more standardized setting in mice made the comparison more striking. In females, R337Q Tregs were sharply reduced in numbers and showed low FoxP3 and CD25 expression, a block in aTreg maturation, and poor ability to colonize non-lymphoid tissues. In males, R337Q Tregs were present in increased numbers, with substantially restored FoxP3 and CD25, increased cell activation, and increased representation in tissues (also with a complete swap in the relative representation of RORg$^+$ and Helios$^+$ subsets of colonic Tregs, in line with the demonstration by us and the Rudensky lab that these subsets have different dependence on FoxP3 function[43,71]). Two core differences between the male and female contexts may explain the divergent outcomes: (1) the presence in heterozygous females of normal Tregs expressing a WT FoxP3, which can outcompete the mutant Tregs for homeostatic niches and trophic factors (in particular IL-2,[3] with a vicious circle where lower access to IL-2 decreased CD25 expression, further reducing IL-2 capture by mutant Tregs), and (2) in males, a strong homeostatic drive that aims to restore Treg function, akin to the strong proliferation observed after acute depletion,[72,73] likely helps to restore mutant Tregs and their maturation and tissue-homing potential (IL-2 produced by dendritic cells or other T cells may be involved here). Is this homeostatic drive and "phenotypic reversion" why males with the mutations are comparatively well off, akin to the aTregs observed in patients?[3] One might also speculate that true sex-specific differences in immune function are at play. Either way, these observations reinforce the notion that the impact of FoxP3 on Treg function is highly context dependent.

How did the mice reproduce the human disease? Some observations did fit: C168Y and F324L showed essentially no phenotype at baseline or when challenged, and we were unable to define any immunologic or transcriptional Treg defect. Patients with these mutations had the mildest symptoms, with late onset and relatively well-tolerated disease. Overall, though, the disease in mice tended to be less severe than in patients, all of which did show the characteristic diagnostic triad. One reason may simply be time (we followed the mice for up to 40 weeks only, shorter than the age at diagnosis for several patients). It is also conceivable that B6 mice are generally more refractory to autoimmunity, and it was interesting that the pancreatic vasculitis of R337Q mice was far more pronounced on the NOD BC1 than B6 backgrounds. The mutation-specific propensity to additional autoimmune diseases like diabetes did not fit (K199del led to pancreatic autoimmunity in mice, but the corresponding patient was not diabetic; the R337Q patient was diabetic). Here, the difference plausibly rests in the complement of autoimmunity susceptibility loci present in the index patients—importantly, islet-specific autoimmunity in K199del BC1 mice remained under the control of MHC alleles, demonstrating the epistasis between *FOXP3* mutations and genetic susceptibility variants.

Limitation of study

The molecular mechanism through which each mutation triggers a different phenotype remains unknown, and we were not able to pinpoint specific transcriptional changes in Tregs induced by the non-FKHR mutations that would connect to the specific autoimmunity they elicit. This may be because the effects are buffered by network regulation and/or only become manifest after challenge (then parsing cause and consequence is difficult). The connection between disease manifestations in humans and mice was not perfect (e.g., most patients presented with enteropathy), possibly due to species differences or other genetic variants at play in these patients.

In conclusion, this work has uncovered unexpected nuances concerning the *in vivo* import of FoxP3's domains in Tregs and how these partake in the interplay between Treg deficiencies, genetic variation, and immunologic challenges that conspire to determine disease manifestations in each patient with IPEX.

STAR★METHODS

Detailed methods are provided in the online version of this paper and include the following:

- KEY RESOURCES TABLE
- RESOURCE AVAILABILITY
  - Lead contact
  - Materials availability
  - Data and code availability
- EXPERIMENTAL MODEL AND SUBJECT DETAILS
  - IPEX human mutations
  - Mice
  - Cell lines
- METHOD DETAILS
  - Mutant mice generation by CRISPR/Cas9
  - Inflammatory challenges
  - Histology
  - ELISA IgE
  - Plasmids

- FoxP3-DNA pulldown assay
- Isolation of lymphocytes from lymphoid and non-lymphoid tissues
- Flow cytometry
- Cell sorting for bulk RNAseq and scATACseq
- Bulk RNA-seq library preparation
- Bulk RNA-seq pre-processing and analysis
- scATAC-seq library preparation
- scATAC hashtagging (ASAP-seq)
- scATAC-seq preprocessing and visualization
- scATAC-seq analysis
- Peak sets
- Motif accessibility analysis
- Gene scores
- Pseudobulk track visualization
- Differential accessibility
- Motif enrichment
- OCR signature relative accessibility

- QUANTIFICATION AND STATISTICAL ANALYSIS

SUPPLEMENTAL INFORMATION

Supplemental information can be found online at https://doi.org/10.1016/j.celrep.2023.113018.

ACKNOWLEDGMENTS

We are grateful to L. Du, Dr. R. Bronson, J. Lee, I. Magill, A. Ciulla, N. Patel, L. Yang, M. Sleeper, C. Araneo, J. Nelson, K. Hattori, V. Piekarsa, and A. Ortiz-Lopez for help with breeding and experimentation and Drs. T. Chatila, L.M. Charbonnier, B. Salomon, and F. Rieux-Laucat for insightful discussions. This work was funded by NIH grants AI-165697 and AI-150686 to C.B. and D.M. and by the JPB Foundation to C.B. and D.M. S.H. is an HHMI investigator, and W.Z. was supported by a Modell fellowship, J.L. by an IMAGINE MD/PhD grant and an Arthur Sachs scholarship, and K.C. by NIGMS fellowships T32GM007753 and T32GM144273 and an HSCI MD/PhD Training Fellowship.

AUTHOR CONTRIBUTIONS

J.L., I.A., and C.B. conceptualized the study. J.L., K.C., W.Z., and R.N.R. performed and analyzed experiments. C.B., D.M., and S.H. supervised. J.L., K.C., and C.B. drafted the manuscript, and all authors edited it.

DECLARATION OF INTERESTS

The authors declare no competing interests.

Received: March 27, 2023
Revised: July 26, 2023
Accepted: August 4, 2023
Published: August 21, 2023

REFERENCES

1. Gavin, M.A., Torgerson, T.R., Houston, E., Deroos, P., Ho, W.Y., Stray-Pedersen, A., Ocheltree, E.L., Greenberg, P.D., Ochs, H.D., and Rudensky, A.Y. (2006). Single-cell analysis of normal and FOXP3-mutant human T cells: FOXP3 expression without regulatory T cell development. Proc. Natl. Acad. Sci. USA *103*, 6659–6664.
2. Di Nunzio, S., Cecconi, M., Passerini, L., McMurchy, A.N., Baron, U., Turbachova, I., Vignola, S., Valencic, E., Tommasini, A., Junker, A., et al. (2009). Wild-type *FOXP3* is selectively active in $CD4^{+}CD25^{hi}$ regulatory T cells of healthy female carriers of different *FOXP3* mutations. Blood *114*, 4138–4141.
3. Zemmour, D., Charbonnier, L.M., Leon, J., Six, E., Keles, S., Delville, M., Benamar, M., Baris, S., Zuber, J., Chen, K., et al. (2021). Single-cell analysis of FOXP3 deficiencies in humans and mice unmasks intrinsic and extrinsic $CD4^{+}$ T cell perturbations. Nat. Immunol. *22*, 607–619.
4. Barzaghi, F., Amaya Hernandez, L.C., Neven, B., Ricci, S., Kucuk, Z.Y., Bleesing, J.J., Nademi, Z., Slatter, M.A., Ulloa, E.R., Shcherbina, A., et al. (2018). Long-term follow-up of IPEX syndrome patients after different therapeutic strategies: An international multicenter retrospective study. J. Allergy Clin. Immunol. *141*, 1036–1049.e5.
5. Jamee, M., Zaki-Dizaji, M., Lo, B., Abolhassani, H., Aghamahdi, F., Mosavian, M., Nademi, Z., Mohammadi, H., Jadidi-Niaragh, F., Rojas, M., et al. (2020). Clinical, Immunological, and Genetic Features in Patients with Immune Dysregulation, Polyendocrinopathy, Enteropathy, X-linked (IPEX) and IPEX-like Syndrome. J. Allergy Clin. Immunol. Pract. *8*, 2747–2760.e7.
6. Sugimoto, N., Oida, T., Hirota, K., Nakamura, K., Nomura, T., Uchiyama, T., and Sakaguchi, S. (2006). Foxp3-dependent and -independent molecules specific for CD25+CD4+ natural regulatory T cells revealed by DNA microarray analysis. Int. Immunol. *18*, 1197–1209.
7. Hill, J.A., Feuerer, M., Tash, K., Haxhinasto, S., Perez, J., Melamed, R., Mathis, D., and Benoist, C. (2007). Foxp3 transcription-factor-dependent and -independent regulation of the regulatory T cell transcriptional signature. Immunity *27*, 786–800.
8. Lin, W., Haribhai, D., Relland, L.M., Truong, N., Carlson, M.R., Williams, C.B., and Chatila, T.A. (2007). Regulatory T cell development in the absence of functional Foxp3. Nat. Immunol. *8*, 359–368.
9. Ohkura, N., Hamaguchi, M., Morikawa, H., Sugimura, K., Tanaka, A., Ito, Y., Osaki, M., Tanaka, Y., Yamashita, R., Nakano, N., et al. (2012). T cell receptor stimulation-induced epigenetic changes and Foxp3 expression are independent and complementary events required for Treg cell development. Immunity *37*, 785–799.
10. Charbonnier, L.M., Cui, Y., Stephen-Victor, E., Harb, H., Lopez, D., Bleesing, J.J., Garcia-Lloret, M.I., Chen, K., Ozen, A., Carmeliet, P., et al. (2019). Functional reprogramming of regulatory T cells in the absence of Foxp3. Nat. Immunol. *20*, 1208–1219.
11. Schubert, L.A., Jeffery, E., Zhang, Y., Ramsdell, F., and Ziegler, S.F. (2001). Scurfin (FOXP3) acts as a repressor of transcription and regulates T cell activation. J. Biol. Chem. *276*, 37672–37679.
12. Bettelli, E., Dastrange, M., and Oukka, M. (2005). Foxp3 interacts with nuclear factor of activated T cells and NF-kappa B to repress cytokine gene expression and effector functions of T helper cells. Proc. Natl. Acad. Sci. USA *102*, 5138–5143.
13. Li, B., Samanta, A., Song, X., Iacono, K.T., Bembas, K., Tao, R., Basu, S., Riley, J.L., Hancock, W.W., Shen, Y., et al. (2007). FOXP3 interactions with histone acetyltransferase and class II histone deacetylases are required for repression. Proc. Natl. Acad. Sci. USA *104*, 4571–4576.
14. Wu, Y., Borde, M., Heissmeyer, V., Feuerer, M., Lapan, A.D., Stroud, J.C., Bates, D.L., Guo, L., Han, A., Ziegler, S.F., et al. (2006). FOXP3 controls regulatory T cell function through cooperation with NFAT. Cell *126*, 375–387.
15. Arvey, A., van der Veeken, J., Samstein, R.M., Feng, Y., Stamatoyannopoulos, J.A., and Rudensky, A.Y. (2014). Inflammation-induced repression of chromatin bound by the transcription factor Foxp3 in regulatory T cells. Nat. Immunol. *15*, 580–587.
16. Chen, C., Rowell, E.A., Thomas, R.M., Hancock, W.W., and Wells, A.D. (2006). Transcriptional regulation by Foxp3 is associated with direct promoter occupancy and modulation of histone acetylation. J. Biol. Chem. *281*, 36828–36834.
17. Ferraro, A., D'Alise, A.M., Raj, T., Asinovski, N., Phillips, R., Ergun, A., Replogle, J.M., Bernier, A., Laffel, L., Stranger, B.E., et al. (2014). Interindividual variation in human T regulatory cells. Proc. Natl. Acad. Sci. USA *111*, E1111–E1120.

18. Kwon, H.K., Chen, H.M., Mathis, D., and Benoist, C. (2017). Different molecular complexes that mediate transcriptional induction and repression by FoxP3. Nat. Immunol. *18*, 1238–1248.

19. Ramirez, R.N., Chowdhary, K., Leon, J., Mathis, D., and Benoist, C. (2022). FoxP3 associates with enhancer-promoter loops to regulate Treg-specific gene expression. Sci. Immunol. *7*, eabj9836.

20. van der Veeken, J., Glasner, A., Zhong, Y., Hu, W., Wang, Z.M., Bou-Puerto, R., Charbonnier, L.M., Chatila, T.A., Leslie, C.S., and Rudensky, A.Y. (2020). The transcription factor Foxp3 shapes regulatory T cell identity by tuning the activity of trans-acting intermediaries. Immunity *53*, 971–984.e5.

21. Ramirez, R.N., Chowdhary, K., and Benoist, C. (2021). Indirect regulation is not the dominant mode of action for the transcription factor FoxP3 in Treg cells. Submitted.

22. Powell, B.R., Buist, N.R., and Stenzel, P. (1982). An X-linked syndrome of diarrhea, polyendocrinopathy, and fatal infection in infancy. J. Pediatr. *100*, 731–737.

23. Wildin, R.S., and Freitas, A. (2005). IPEX and FOXP3: clinical and research perspectives. J. Autoimmun. *25*, 56–62.

24. Barzaghi, F., Passerini, L., and Bacchetta, R. (2012). Immune dysregulation, polyendocrinopathy, enteropathy, x-linked syndrome: a paradigm of immunodeficiency with autoimmunity. Front. Immunol. *3*, 211.

25. Duclaux-Loras, R., Charbit-Henrion, F., Neven, B., Nowak, J., Collardeau-Frachon, S., Malcus, C., Ray, P.F., Moshous, D., Beltrand, J., Goulet, O., et al. (2018). Clinical Heterogeneity of Immune Dysregulation, Polyendocrinopathy, Enteropathy, X-Linked Syndrome: A French Multicenter Retrospective Study. Clin. Transl. Gastroenterol. *9*, 201.

26. Gambineri, E., Ciullini Mannurita, S., Hagin, D., Vignoli, M., Anover-Sombke, S., DeBoer, S., Segundo, G.R.S., Allenspach, E.J., Favre, C., Ochs, H.D., and Torgerson, T.R. (2018). Clinical, immunological, and molecular heterogeneity of 173 patients with the phenotype of Immune Dysregulation, Polyendocrinopathy, Enteropathy, X-Linked (IPEX) syndrome. Front. Immunol. *9*, 2411.

27. McMurchy, A.N., Gillies, J., Allan, S.E., Passerini, L., Gambineri, E., Roncarolo, M.G., Bacchetta, R., and Levings, M.K. (2010). Point mutants of forkhead box P3 that cause immune dysregulation, polyendocrinopathy, enteropathy, X-linked have diverse abilities to reprogram T cells into regulatory T cells. J. Allergy Clin. Immunol. *126*, 1242–1251.

28. Wiesmann, C., Katschke, K.J., Yin, J., Helmy, K.Y., Steffek, M., Fairbrother, W.J., McCallum, S.A., Embuscado, L., DeForge, L., Hass, P.E., and van Lookeren Campagne, M. (2006). Structure of C3b in complex with CRIg gives insights into regulation of complement activation. Nature *444*, 217–220.

29. Lin, W., Truong, N., Grossman, W.J., Haribhai, D., Williams, C.B., Wang, J., Martín, M.G., and Chatila, T.A. (2005). Allergic dysregulation and hyperimmunoglobulinemia E in Foxp3 mutant mice. J. Allergy Clin. Immunol. *116*, 1106–1115.

30. Hayatsu, N., Miyao, T., Tachibana, M., Murakami, R., Kimura, A., Kato, T., Kawakami, E., Endo, T.A., Setoguchi, R., Watarai, H., et al. (2017). Analyses of a mutant Foxp3 allele reveal BATF as a critical transcription factor in the differentiation and accumulation of tissue regulatory T cells. Immunity *47*, 268–283.e9.

31. Kwon, H.K., Chen, H.M., Mathis, D., and Benoist, C. (2018). FoxP3 scanning mutagenesis reveals functional variegation and mild mutations with atypical autoimmune phenotypes. Proc. Natl. Acad. Sci. USA *115*, E253–E262.

32. Van Gool, F., Nguyen, M.L.T., Mumbach, M.R., Satpathy, A.T., Rosenthal, W.L., Giacometti, S., Le, D.T., Liu, W., Brusko, T.M., Anderson, M.S., et al. (2019). A mutation in the transcription factor Foxp3 drives T helper 2 effector function in regulatory T cells. Immunity *50*, 362–377.e6.

33. Leng, F., Zhang, W., Ramirez, R.N., Leon, J., Zhong, Y., Hou, L., Yuki, K., van der Veeken, J., Benoist, C., Hur, S., Rudensky, A.Y., and Benoist, C. (2022). The transcription factor FoxP3 can fold into two dimerization states with divergent implications for regulatory T cell function and immune homeostasis. Immunity *55*, 1354–1369.e8.

34. Bacchetta, R., Passerini, L., Gambineri, E., Dai, M., Allan, S.E., Perroni, L., Dagna-Bricarelli, F., Sartirana, C., Matthes-Martin, S., et al. (2006). Defective regulatory and effector T cell functions in patients with FOXP3 mutations. J. Clin. Invest. *116*, 1713–1722.

35. Zemmour, D., Zilionis, R., Kiner, E., Klein, A.M., Mathis, D., and Benoist, C. (2018). Single-cell gene expression reveals a landscape of regulatory T cell phenotypes shaped by the TCR. Nat. Immunol. *19*, 291–301.

36. Bettelli, E., Carrier, Y., Gao, W., Korn, T., Strom, T.B., Oukka, M., Weiner, H.L., and Kuchroo, V.K. (2006). Reciprocal developmental pathways for the generation of pathogenic effector TH17 and regulatory T cells. Nature *441*, 235–238.

37. Bandukwala, H.S., Wu, Y., Feuerer, M., Chen, Y., Barboza, B., Ghosh, S., Stroud, J.C., Benoist, C., Mathis, D., Rao, A., and Chen, L. (2011). Structure of a domain-swapped FOXP3 dimer on DNA and its function in regulatory T cells. Immunity *34*, 479–491.

38. Herman, A.E., Freeman, G.J., Mathis, D., and Benoist, C. (2004). CD4+CD25+ T regulatory cells dependent on ICOS promote regulation of effector cells in the prediabetic lesion. J. Exp. Med. *199*, 1479–1489.

39. Josefowicz, S.Z., Lu, L.F., and Rudensky, A.Y. (2012). Regulatory T cells: mechanisms of differentiation and function. Annu. Rev. Immunol. *30*, 531–564.

40. Joller, N., Lozano, E., Burkett, P.R., Patel, B., Xiao, S., Zhu, C., Xia, J., Tan, T.G., Sefik, E., Yajnik, V., et al. (2014). Treg cells expressing the coinhibitory molecule TIGIT selectively inhibit proinflammatory Th1 and Th17 cell responses. Immunity *40*, 569–581.

41. Gavin, M.A., Rasmussen, J.P., Fontenot, J.D., Vasta, V., Manganiello, V.C., Beavo, J.A., and Rudensky, A.Y. (2007). Foxp3-dependent programme of regulatory T-cell differentiation. Nature *445*, 771–775.

42. Traxinger, B.R., Richert-Spuhler, L.E., and Lund, J.M. (2022). Mucosal tissue regulatory T cells are integral in balancing immunity and tolerance at portals of antigen entry. Mucosal Immunol. *15*, 398–407.

43. Chowdhary, K., Léon, J., Ramanan, D., Mathis, D., and Benoist, C. (2023). An interwoven network of transcription factors, with divergent influences from FoxP3, underlies Treg diversity. Preprint at bioRxiv. https://doi.org/10.1101/2023.05.18.541358.

44. Benoist, C., and Mathis, D. (2013). Treg cells, life history, and diversity. In Immune Tolerance, D. Mathis and A. Rudensky, eds. (Cold Spring Harbor Press), pp. 31–44.

45. Wildin, R.S., Smyk-Pearson, S., and Filipovich, A.H. (2002). Clinical and molecular features of the immunodysregulation, polyendocrinopathy, enteropathy, X linked (IPEX) syndrome. J. Med. Genet. *39*, 537–545.

46. Singh, N., Chandler, P.R., Seki, Y., Baban, B., Takezaki, M., Kahler, D.J., Munn, D.H., Larsen, C.P., Mellor, A.L., and Iwashima, M. (2007). Role of CD28 in fatal autoimmune disorder in *scurfy* mice. Blood *110*, 1199–1206.

47. Sharma, R., Sung, S.S.J., Gaskin, F., Fu, S.M., and Ju, S.T. (2012). A novel function of IL-2: chemokine/chemoattractant/retention receptor genes induction in Th subsets for skin and lung inflammation. J. Autoimmun. *38*, 322–331.

48. Chassaing, B., Aitken, J.D., Malleshappa, M., and Vijay-Kumar, M. (2014). Dextran sulfate sodium (DSS)-induced colitis in mice. Curr. Protoc. Im. *104*. Unit.

49. Li, M., Hener, P., Zhang, Z., Kato, S., Metzger, D., and Chambon, P. (2006). Topical vitamin D3 and low-calcemic analogs induce thymic stromal lymphopoietin in mouse keratinocytes and trigger an atopic dermatitis. Proc. Natl. Acad. Sci. USA *103*, 11736–11741.

50. Acha-Orbea, H., and McDevitt, H.O. (1987). The first external domain of the nonobese diabetic mouse class II I-A beta chain is unique. Proc. Natl. Acad. Sci. USA *84*, 2435–2439.

51. Pearson, J.A., Wong, F.S., and Wen, L. (2016). The importance of the Non Obese Diabetic (NOD) mouse model in autoimmune diabetes. J. Autoimmun. *66*, 76–88.

52. Wang, L., Ray, A., Jiang, X., Wang, J.Y., Basu, S., Liu, X., Qian, T., He, R., Dittel, B.N., and Chu, Y. (2015). T regulatory cells and B cells cooperate to form a regulatory loop that maintains gut homeostasis and suppresses dextran sulfate sodium-induced colitis. Mucosal Immunol. *8*, 1297–1312.

53. Sefik, E., Geva-Zatorsky, N., Oh, S., Konnikova, L., Zemmour, D., McGuire, A.M., Burzyn, D., Ortiz-Lopez, A., Lobera, M., Yang, J., et al. (2015). Individual intestinal symbionts induce a distinct population of RORγ$^+$ regulatory T cells. Science *349*, 993–997.

54. Makino, S., Muraoka, Y., Kishimoto, Y., and Hayashi, Y. (1985). Genetic analysis for insulitis in NOD mice. Jikken Dobutsu *34*, 425–431.

55. Wicker, L.S., Miller, B.J., Coker, L.Z., McNally, S.E., Scott, S., Mullen, Y., and Appel, M.C. (1987). Genetic control of diabetes and insulitis in the non-obese diabetic (NOD) mouse. J. Exp. Med. *165*, 1639–1654.

56. André, I., Gonzalez, A., Wang, B., Katz, J., Benoist, C., and Mathis, D. (1996). Checkpoints in the progression of autoimmune disease: lessons from diabetes models. Proc. Natl. Acad. Sci. USA *93*, 2260–2263.

57. McDevitt, H.O. (1998). The role of MHC class II molecules in susceptibility and resistance to autoimmunity. Curr. Opin. Immunol. *10*, 677–681.

58. Wildin, R.S., Ramsdell, F., Peake, J., Faravelli, F., Casanova, J.L., Buist, N., Levy-Lahad, E., Mazzella, M., Goulet, O., Perroni, L., et al. (2001). X-linked neonatal diabetes mellitus, enteropathy and endocrinopathy syndrome is the human equivalent of mouse scurfy. Nat. Genet. *27*, 18–20.

59. Mimitou, E.P., Lareau, C.A., Chen, K.Y., Zorzetto-Fernandes, A.L., Hao, Y., Takeshima, Y., Luo, W., Huang, T.S., Yeung, B.Z., Papalexi, E., et al. (2021). Scalable, multimodal profiling of chromatin accessibility, gene expression and protein levels in single cells. Nat. Biotechnol. *39*, 1246–1258.

60. Schep, A.N., Wu, B., Buenrostro, J.D., and Greenleaf, W.J. (2017). ChromVAR: inferring transcription-factor-associated accessibility from single-cell epigenomic data. Nat. Methods *14*, 975–978.

61. Feng, Y., Arvey, A., Chinen, T., van der Veeken, J., Rudensky, A.Y., Gasteiger, G., and Rudensky, A.Y. (2014). Control of the inheritance of regulatory T cell identity by a cis element in the Foxp3 locus. Cell *158*, 749–763.

62. Li, X., Liang, Y., LeBlanc, M., Benner, C., and Zheng, Y. (2014). Function of a Foxp3 cis-element in protecting regulatory T cell identity. Cell *158*, 734–748.

63. Grant, F.M., Yang, J., Nasrallah, R., Clarke, J., Sadiyah, F., Whiteside, S.K., Imianowski, C.J., Kuo, P., Vardaka, P., Todorov, T., et al. (2020). BACH2 drives quiescence and maintenance of resting Treg cells to promote homeostasis and cancer immunosuppression. J. Exp. Med. *217*, e20190711.

64. Rudra, D., Deroos, P., Chaudhry, A., Niec, R.E., Arvey, A., Samstein, R.M., Leslie, C., Shaffer, S.A., Goodlett, D.R., and Rudensky, A.Y. (2012). Transcription factor Foxp3 and its protein partners form a complex regulatory network. Nat. Immunol. *13*, 1010–1019.

65. Samstein, R.M., Arvey, A., Josefowicz, S.Z., Peng, X., Reynolds, A., Sandstrom, R., Neph, S., Sabo, P., Kim, J.M., Liao, W., et al. (2012). Foxp3 exploits a pre-existent enhancer landscape for regulatory T cell lineage specification. Cell *151*, 153–166.

66. Tsuda, M., Torgerson, T.R., Selmi, C., Gambineri, E., Carneiro-Sampaio, M., Mannurita, S.C., Leung, P.S.C., Norman, G.L., and Gershwin, M.E. (2010). The spectrum of autoantibodies in IPEX syndrome is broad and includes anti-mitochondrial autoantibodies. J. Autoimmun. *35*, 265–268.

67. Ge, T., Wang, Y., Che, Y., Xiao, Y., and Zhang, T. (2017). Atypical Late-Onset Immune Dysregulation, Polyendocrinopathy, Enteropathy, X-Linked Syndrome with Intractable Diarrhea: A Case Report. Front. Pediatr. *5*, 267.

68. Al Maawali, A., Derfalvi, B., Van Limbergen, J., Issekutz, A., Issekutz, T., Ghandourah, H., and Rashid, M. (2020). IPEX Syndrome with Normal FOXP3 Protein Expression in Treg Cells in an Infant Presenting with Intractable Diarrhea as a Single Symptom. Case Reports Immunol. *2020*, 9860863.

69. Darce, J., Rudra, D., Li, L., Nishio, J., Cipolletta, D., Rudensky, A.Y., Mathis, D., and Benoist, C. (2012). An N-terminal mutation of the Foxp3 transcription factor alleviates arthritis but exacerbates diabetes. Immunity *36*, 731–741.

70. Bettini, M.L., Pan, F., Bettini, M., Finkelstein, D., Rehg, J.E., Floess, S., Bell, B.D., Ziegler, S.F., Huehn, J., Pardoll, D.M., and Vignali, D.A.A. (2012). Loss of epigenetic modification driven by the Foxp3 transcription factor leads to regulatory T cell insufficiency. Immunity *36*, 717–730.

71. van der Veeken, J., Campbell, C., Pritykin, Y., Schizas, M., Verter, J., Hu, W., Wang, Z.M., Matheis, F., Mucida, D., Charbonnier, L.M., et al. (2022). Genetic tracing reveals transcription factor Foxp3-dependent and Foxp3-independent functionality of peripherally induced Treg cells. Immunity *55*, 1173–1184.e7.

72. Kim, J.M., Rasmussen, J.P., and Rudensky, A.Y. (2007). Regulatory T cells prevent catastrophic autoimmunity throughout the lifespan of mice. Nat. Immunol. *8*, 191–197.

73. Feuerer, M., Shen, Y., Littman, D.R., Benoist, C., and Mathis, D. (2009). How punctual ablation of regulatory T cells unleashes an autoimmune lesion within the pancreatic islets. Immunity *31*, 654–664.

74. Makino, S., Kunimoto, K., Muraoka, Y., Mizushima, Y., Katagiri, K., and Tochino, Y. (1980). Breeding of a non-obese, diabetic strain of mice. Exp. Anim. *29*, 1–13.

75. Liston, A., Nutsch, K.M., Farr, A.G., Lund, J.M., Rasmussen, J.P., Koni, P.A., and Rudensky, A.Y. (2008). Differentiation of regulatory Foxp3$^+$ T cells in the thymic cortex. Proc. Natl. Acad. Sci. USA *105*, 11903–11908.

76. Granja, J.M., Corces, M.R., Pierce, S.E., Bagdatli, S.T., Choudhry, H., Chang, H.Y., and Greenleaf, W.J. (2021). ArchR is a scalable software package for integrative single-cell chromatin accessibility analysis. Nat. Genet. *53*, 403–411.

77. Stuart, T., Srivastava, A., Madad, S., Lareau, C.A., and Satija, R. (2021). Single-cell chromatin state analysis with Signac. Nat. Methods *18*, 1333–1341.

78. Hao, Y., Hao, S., Andersen-Nissen, E., Mauck, W.M., III, Zheng, S., Butler, A., Lee, M.J., Wilk, A.J., Darby, C., Zager, M., et al. (2021). Integrated analysis of multimodal single-cell data. Cell *184*, 3573–3587.e29.

79. Ramírez, F., Ryan, D.P., Grüning, B., Bhardwaj, V., Kilpert, F., Richter, A.S., Heyne, S., Dündar, F., and Manke, T. (2016). deepTools2: a next generation web server for deep-sequencing data analysis. Nucleic Acids Res. *44*, W160–W165.

80. Robinson, J.T., Thorvaldsdóttir, H., Winckler, W., Guttman, M., Lander, E.S., Getz, G., and Mesirov, J.P. (2011). Integrative genomics viewer. Nat. Biotechnol. *29*, 24–26.

81. Zemmour, D., Pratama, A., Loughhead, S.M., Mathis, D., and Benoist, C. (2017). Flicr, a long noncoding RNA, modulates Foxp3 expression and autoimmunity. Proc. Natl. Acad. Sci. USA *114*, E3472–E3480.

82. Cusanovich, D.A., Hill, A.J., Aghamirzaie, D., Daza, R.M., Pliner, H.A., Berletch, J.B., Filippova, G.N., Huang, X., Christiansen, L., DeWitt, W.S., et al. (2018). A Single-Cell Atlas of In Vivo Mammalian Chromatin Accessibility. Cell *174*, 1309–1324.e18.

83. Stuart, T., Butler, A., Hoffman, P., Hafemeister, C., Papalexi, E., Mauck, W.M., III, Hao, Y., Stoeckius, M., Smibert, P., and Satija, R. (2019). Comprehensive integration of single-cell data. Cell *177*, 1888–1902.e21.

84. McInnes, L., Healy, J., and Mellvile, J. (2018). UMAP: Uniform Manifold Approximation and Projection for Dimension Reduction. Preprint at arXiv. https://doi.org/10.48550/arXiv.1802.03426.

85. Melsted, P., Booeshaghi, A.S., Liu, L., Gao, F., Lu, L., Min, K.H.J., da Veiga Beltrame, E., Hjörleifsson, K.E., Gehring, J., and Pachter, L. (2021).

Modular, efficient and constant-memory single-cell RNA-seq preprocessing. Nat. Biotechnol. *39*, 813–818.

86. Booeshaghi, A.S., Min, K.H., Gehring, J., and Pachter, L. (2022). Quantifying orthogonal barcodes for sequence census assays. Preprint at bioRxiv. https://doi.org/10.1101/2022.10.09.511501.
87. Stoeckius, M., Hafemeister, C., Stephenson, W., Houck-Loomis, B., Chattopadhyay, P.K., Swerdlow, H., Satija, R., and Smibert, P. (2017). Simultaneous epitope and transcriptome measurement in single cells. Nat. Methods *14*, 865–868.
88. Yoshida, H., Lareau, C.A., Ramirez, R.N., Rose, S.A., Maier, B., Wroblewska, A., Desland, F., Chudnovskiy, A., Mortha, A., Dominguez, C., et al. (2019). The cis-Regulatory Atlas of the Mouse Immune System. Cell *176*, 897–912.e20.

STAR★METHODS

KEY RESOURCES TABLE

REAGENT or RESOURCE	SOURCE	IDENTIFIER
Antibodies		
BV605 anti-mouse CD45 (clone 30-F11)	Biolegend	Cat# 103140
AF700 anti-Mouse TCRβ (clone H57-597)	Biolegend	Cat# 109224
BUV737 anti-Mouse TCRβ (clone H57-597)	BD	Cat# 612821
BUV737 anti-Mouse NK1.1 (clone PK136)	BD	Cat# 741715
PE-eFluor™ 610 anti-mouse CD4 (clone RM4-5)	Invitrogen	Cat# 61-0042-82
PE/Cyanine7 anti-mouse CD4 (clone RM4-5)	Biolegend	Cat# 100528
AF700 anti-mouse CD8a (clone 53–5.8)	Biolegend	Cat# 100730
BV605 anti-mouse CD19 (clone 6D5)	Biolegend	Cat# 115540
APC anti-rat CD90/mouse CD90.1 (clone OX-7)	Biolegend	Cat# 202526
PE/Cyanine7 anti-rat CD90/mouse CD90.1 (clone OX-7)	Biolegend	Cat# 202518
PerCP/Cyanine5.5 anti-mouse/human CD44 (clone IM7)	Biolegend	Cat# 103032
BV510 anti-mouse/human CD44 (clone IM7)	Biolegend	Cat# 103044
PE/Cyanine7 anti-mouse CD62L (clone MEL-14)	Biolegend	Cat# 104418
BV785 anti-mouse CD62L (clone MEL-14)	Biolegend	Cat# 104440
BV785 anti-mouse CCR2 (cloneSA203G11)	Biolegend	Cat# 150621
BV510 anti-mouse CXCR3 (clone CXCR3-173)	Biolegend	Cat# 126528
BV785 anti-mouse CXCR5 (clone L138D7)	Biolegend	Cat# 145523
APC anti-mouse CXCR6 (clone SA051D1)	Biolegend	Cat# 151106
PE anti-mouse CD11b (clone M1/70)	Biolegend	Cat# 101208
PE-eFluor™ 610 anti-mouse CD11c (clone N418)	Invitrogen	Cat# 61-0114-82
Pacific Blue anti-mouse CD3 (clone 17AE)	Biolegend	Cat# 100214
PE-eFluor™ 610 anti-mouse KLRG1 (clone 2F1)	Invitrogen	Cat# 61-5893-82
PE/Cyanine7 anti-mouse PD-1 (clone 29F.1A12)	Biolegend	Cat# 135216
PE anti-mouse CD25 (clone PC-61)	Biolegend	Cat# 102008
Pacific Blue anti-mouse CD103 (clone 2E7)	Biolegend	Cat# 121418
BV605 anti-mouse CTLA-4 (clone UC10-4B9)	Biolegend	Cat# 106323
Pacific Blue anti-mouse Helios (clone 22F6)	Biolegend	Cat# 137220
APC anti-Foxp3 (clone FJK-16s)	eBioscience	Cat# 17-5773-82
AF488 anti-Foxp3 (clone FJK-16s)	eBioscience	Cat# 53-5773-82
PE anti-RORγt (clone AFKJS-9)	eBioscience	Cat# 12-6988-82
APC anti-RORγt (clone AFKJS-9)	eBioscience	Cat# 17-6988-82
PE-eFluor™ 610 anti-Gata3 (clone TWAJ)	eBioscience	Cat# 61-9966-42
AF700 anti-Ki-67 (clone 16A8)	Biolegend	Cat# 652419

(*Continued on next page*)

Continued

REAGENT or RESOURCE	SOURCE	IDENTIFIER
TotalSeq-A anti-mouse hashtags (1,6,9,10,12)	Biolegend	Cat# 155801 Cat# 155811 Cat# 155817 Cat# 155819 Cat# 155823
Chemicals, peptides, and recombinant proteins		
Alt-R S.p. HiFi Caspase 9 Nuclease V3	IDT	Cat# 1081060
Phusion® High-Fidelity DNA Polymerase	NEB	Cat# M0530L
DreamTaq DNA Polymerase	Thermo Fisher	EP0702
DreamTaq PCR Master Mix	Thermo Fisher	K1071
PstI restriction endonuclease	NEB	Cat# R0140S
SmaI restriction endonuclease	NEB	Cat# R0141S
AvaI restriction endonuclease	NEB	Cat# R0152S
BglII restriction endonuclease	NEB	Cat# R0144S
NdeI restriction endonuclease	NEB	Cat# R0111S
Collagenase type II (Gibco)	Thermo Fisher	Cat# 17101015
Collagenase type II	Sigma-Aldrich	Cat# C6885-5G
Collagenase type IV	Sigma-Aldrich	Cat# C5138-1G
Hyaluronidase from bovine testes	Sigma-Aldrich	Cat# H3884
Dispase (Gibco)	Thermo Fisher	Cat# 17105041
DNase I, from bovine pancreas	Sigma-Aldrich	Cat# D4527
Benzonase	Millipore	Cat# 70664
Anti-HA Magnetic Beads	Thermo Fisher	Cat#88837
Proteinase K	NEB	Cat# P8107S
Dextran Sulfate Sodium (DSS)	Thermo Fisher	Cat# J62101.22
Calcipotriol (MC903)	MedChemExpress	Cat# HY-10001
10% Neutral Buffered Formalin	eBioscience	Cat# 00-4980-03
Bouin's solution	VWR	Cat# 15990-01
2-Mercaptoethanol	Sigma-Aldrich	Cat# M7522
TCL RNA lysis buffer	Qiagen	Cat# 1031576
10% Novex TBE Gels	Invitrogen	Cat#EC62755BOX
TE Buffer	Invitrogen	Cat# 12090015
ACK lysis buffer	Gibco	Cat# A10492-01
Critical commercial assays		
Foxp3/Transcription Factor Staining Buffer Set	eBioscience	Cat# 00-5523-00
LIVE/DEAD™ Fixable Near IR (780) Viability Kit	Invitrogen	Cat# L34994
IgE Mouse Uncoated ELISA Kit	Thermo Fisher	Cat # 88-50460-22
QIAquick Gel Extraction Kit	QIAGEN	Cat # 28706
QIAquick Nucleotide Removal kit	QIAGEN	Cat# 28306
Chromium Next GEM Single Cell ATAC	10x Genomics	Cat# 1000176
Deposited data		
scATAC-seq of splenic mutant Tregs	This manuscript	GEO: GSE237198
Bulk RNA-seq of splenic mutant Tregs (R51Q,C168Y,K199del,R309Q, F324L,R337Q)	This manuscript	GEO: GSE225891
Bulk RNA-seq of Foxp3^{+} regulatory T cells and Foxp3 reporter-null cells	van der Veeken et al. [20]	GEO: GSE154680
Gene expression by array of splenic mutant Tregs (I363V, A384T, R397W)	Hayatsu et al.[30]	GEO: GSE89654

(*Continued on next page*)

Continued

REAGENT or RESOURCE	SOURCE	IDENTIFIER
Experimental models: Cell lines		
HEK293T	ATCC	CRL-11268
Experimental models: Organisms/strains		
Mouse: C57BL/6J	Jackson Laboratory	000664
Mouse: NOD/LtJ.DOI	Makino et al.[74]	From our Colony
Mouse: B6.Foxp3IRES-GFP	Bettelli et al.[36]	From our Colony
Mouse: B6.Foxp3Thy1.1	Liston et al.[75]	From our Colony
Mouse: B6.Foxp3fs327-GFP	Ricardo et al.[19]	From our Colony
Mouse: B6. Foxp3R51Q	This manuscript	From our Colony
Mouse: B6. Foxp3C168Y	This manuscript	From our Colony
Mouse: B6. Foxp3K199del	This manuscript	From our Colony
Mouse: B6. Foxp3R309Q	This manuscript	From our Colony
Mouse: B6. Foxp3F324L	This manuscript	From our Colony
Mouse: B6. Foxp3R337Q	This manuscript	From our Colony
Oligonucleotides		
pcDNA-HA-FoxP3	Leng et al. 2022[33]	N/A
pcDNA-HA-FoxP3-R51Q	This manuscript	N/A
pcDNA-HA-FoxP3-C168Y	This manuscript	N/A
pcDNA-HA-FoxP3-K199del	This manuscript	N/A
pcDNA-HA-FoxP3-R309Q	This manuscript	N/A
pcDNA-HA-FoxP3-F324L	This manuscript	N/A
pcDNA-HA-FoxP3-R337Q	This manuscript	N/A
Customed Alt-R™ HDR Donor Oligo	IDT	N/A
Customed Alt-R® CRISPR-Cas9 crRNA	IDT	N/A
Alt-R® CRISPR-Cas9 tracrRNA, 20 nmol	IDT	Cat# 1072533
Software and algorithms		
R studio software v2022.12.0 + 353	The R Foundation	https://www.r-project.org/
Python software v3.9.7	Python	https://www.python.org/
Cell Ranger ATAC software v1.2	10x Genomics	N/A
ArchR v1.0.1	Granja et al.[76]	https://www.archrproject.com/
Signac v1.4	Stuart et al.[77]	https://stuartlab.org/signac/
ASAP-seq	Mimitou et al.[59]	https://github.com/caleblareau/asap_to_kite
Seurat package (v4.0.2)	Hao et al.[78]	https://satijalab.org/seurat/
ChromVar v1.4.1	Schep et al.[60]	N/A
deeptools v3.0.2	Ramirez et al.[79]	N/A
IGV v2.4.14	Robinson et al.[80]	N/A
GenePattern software package	Broad Institute	http://software.broadinstitute.org/cancer/software/genepattern/
PRISM v9.5.0	GraphPad	https://www.graphpad.com/
FlowJo 10.7	BD Biosciences	https://www.flowjo.com/

RESOURCE AVAILABILITY

Lead contact

Further information and requests for resources and reagents should be directed to and will be fulfilled by the lead contact, Christophe Benoist (cb@hms.harvard.edu).

Materials availability

Mouse lines generated in this study have been cryopreserved and will be made available to qualified investigators upon justified request to the lead contact.

Data and code availability

Data newly reported in this manuscript, BulkRNAseq and scATAC-seq data, have been deposited at the Gene Expression Omnibus and are publicly available as of the date of publication. This paper also analyzes existing, publicly available data. Accession numbers are listed in the key resources table.

This paper does not report original code.

Any additional information required to reanalyze the data reported in this paper is available from the lead contact upon request.

EXPERIMENTAL MODEL AND SUBJECT DETAILS

IPEX human mutations

The 6 mutations from IPEX patients (Table S1) were previously reported in Zemmour et al.[3]: R51Q, C168Y (C169Y in human FOXP3), K199del (K200del in human FOXP3), R309Q and R337Q; or in Bacchetta et al[34].

Mice

C57Bl/6J (B6) mice were purchased from the Jackson Laboratory. *Foxp3*$^{IRES-GFP}$,[36] Foxp3$^{Thy1.1}$[75] and *Foxp3*$^{fs327-GFP}$[19] mice on the B6 background, and NOD/LtJ.DOI (NOD) mice were maintained in our laboratory. Except when specified, 6 to 10-wk-old male and female mice were used in experiments. They originated from breeding of heterozygous Foxp3$^{Mutant/WT}$ females with Foxp3$^{WT-Thy1.1}$ males, to generate both mutants and WT littermate controls from the same cage, female or male. For backcross to the NOD background, mutant males were crossed with NOD females to generate heterozygous Foxp3$^{mutant/WT}$ F1 females, which were then crossed to NOD male. All mice were housed under specific pathogen-free conditions and all experiments were performed in accordance with guidelines from the Institutional Animal Care Committee of Harvard Medical School (protocol #IS00001257).

Cell lines

For transfection, HEK293T cells were purchased from ATCC (CRL-11268), and Cells were maintained in DMEM (High glucose, L-glutamine, Pyruvate) with 10% fetal bovine serum, 1% penicillin/streptomycin.

METHOD DETAILS

Mutant mice generation by CRISPR/Cas9

Mutant mice were generated by CRISPR mutagenesis, essentially as described,[81] except that the micro-injected complex included recombinant Cas9 (0.13μM Alt-R S.p. HiFi Caspase 9; IDT), 0.6μM sgRNA (IDT), and 0.3μM of a single stranded recombination template carrying the desired mutation with 60 bp of flanking homology arms, mixed in 0.2μm-filtered 0.1X TE Buffer). This mix was microinjected into the male pronucleus of fertilized mouse oocytes, which were then implanted into pseudo-pregnant females.

To generate fertilized oocytes, we used males from the *Foxp3*$^{IRES-GFP}$[36] knockin in order to insert the mutation directly into this tagged locus. However, this strategy was successful only in half of the mutation generation, for R51Q, K199del and F324L. The failures were, a posteriori, explained by the fact that the mix likely leaked into the cytoplasm and the mutation was ultimately inserted into the non-tagged female genetic material. Two independent founders carrying the R51Q mutation were obtained, one in the normal allele, one in the GFP-tagged allele; the former was used for most experiments.

To facilitate further mouse genotyping, we added a silent mutation in each mutated template, introducing or deleting a restriction enzyme site. The mutation and the remainder of the FoxP3-coding region were verified by PCR amplification and Sanger sequencing after using a DNA gel extraction kit (Qiagen). Genotyping of each strain was performed by PCR amplification around the mutated and subsequent restriction enzyme digestion was done. If there were doubt about the digestion, the genotype was further verified by Sanger sequencing of the amplicon. The PCR primers as well as the enzyme restriction used for each line for genotyping are described in Table S1. Genotyping of BC1 mice at MHC-II loci (H2-A$^{g7/g7}$ or H2-A$^{b'g7}$) was done by PCR amplification and Sanger sequencing, based on sequences from ref. [50].

Inflammatory challenges

For DSS treatment, 2.5% DSS (Thermo Scientific) was provided in the drinking water from day 0 to day 6 and mice were followed until day 10 (weight and clinical state).

For MC903 treatment, 3 nmol of calcitriol dissolved in 70% ethanol (10mg stock, MedChemExpress – Cat# HY-10001) was administered topically to the dorsal and ventral aspects of the skin of one adult mice ear, daily, for 10 days and then mice were followed until day 25. Mice were monitored once per day for ear local inflammation, which was scored based on the ear thickness, measured using a caliper – as a proportion of increase (%) from the non-injured D0 measure.

Histology

All tissues were collected and fixed in 10% formalin at least 24 h, except the colon which was fixed in Bouin solution. Tissues were embedded in paraffin and processed at the HMS Rodent Histopathology for hematoxylin and eosin (H&E) staining. Images were acquired with a Nikon Ti inverted microscope at ×10 magnification. For general grading tissue immune infiltration, evaluation from H&E sections was performed in a blinded fashion by an independent pathologist at the HMS Rodent Histopathology Core. For insulitis, several islets (>15) were scored for each mouse (where 0: normal; 1: peri-insulitis, accumulation around the islet but no breach of the islet capsule; 2; clear insulitis, inflammatory cells invading and in contact with β-cells; 3: severe insulitis, >50% of the islet taken over or destroyed) Perivascular inflammation in the connective/ductal spaces of the pancreas (observed in R337Q mice) was scored as 0: no inflammation; 1: clear perivascular infiltrates, intact acinar or islet tissue; 2: abundant perivascular infiltrates, with destruction of the surrounding acinar tissue, but large areas of the pancreas still present; 3: severe, quasi-complete destruction of the exocrine pancreas.

ELISA IgE

IgE concentrations were measured by commercial ELISA kit according to the manufacturer's recommendations (Thermo Fisher Scientific), after plasma dilution at 1:50 to 1:100.

Plasmids

For Mammalian expression plasmids, HA-tagged mouse FoxP3 CDS was inserted into pcDNA3.1+ vector between KpnI and BamHI sites. All FoxP3 mutations including R51Q, C168Y, K199del, R309Q, F324L and R337Q were generated by site-directed mutagenesis using Phusion High Fidelity (New England Biolabs) DNA polymerases.

FoxP3-DNA pulldown assay

HEK293T cells were transfected with pcDNA encoding HA-tagged FoxP3 (wild-type or mutants). After 48 h, cells were lysed using RIPA buffer (10mM Tris-HCl, pH 8.0, 1mM EDTA, 1% Triton X-100, 0.1% Sodium Deoxycholate, 0.1% SDS, 140 mM NaCl and 1x proteinase inhibitor) and treated with Benzonase (Millipore) for 30 min. The lysate was then incubated with Anti-HA Magnetic Beads (Thermo Fisher) for 1 h. Beads were washed three times using RIPA buffer and incubated with IR-FKHM^{4g} (TAGGAAAATT**TGTTTAC** TCGA**GTAAACA** TC) for 20 min at room temperature. Bound DNA was recovered using proteinase K (New England Biolabs), purified using QIAquick Nucleotide Removal kit (QIAGEN) and analyzed on 10% Novex TBE Gels (Invitrogen).

Isolation of lymphocytes from lymphoid and non-lymphoid tissues

Spleen and lymph nodes

Immunocytes were released using mechanical disruption followed by filtering and washes in FACS Buffer (phenol red-free DMEM (Gibco) containing 2% fetal calf serum (FCS)). Additional step for red blood cell lysis in spleen samples was performed using ACK lysis buffer (Gibco, ref A10492-01).

Colon

intestinal tissues were measured, cleaned, and incubated in RPMI (Gibco) containing 1 mM dithiothreitol, 20 mM EDTA, and 2% FBS at 37°C for 15 min to remove epithelial cells. The colon was then minced and dissociated in RPMI containing 1.5 mg/mL collagenase II (Gibco), 0.5 mg/mL Dispase (Gibco), and 1% FCS, at 37°C for 45 min with constant stirring. The digested materials were filtered through a 40-μm cell strainer, washed with 2% FBS-RPMI and resuspended in FACS buffer.

Lungs

the right lobe of the lungs was collected, minced and dissociated in collagenase solution (1 mg/mL collagenase type IV (Sigma), 150 μg/mL DNase I (Sigma) and 1% FCS in RPMI) and incubated in a water bath at 37°C with constant shaking for 30 min. Digested tissues were filtered through a 40-μm cell strainer and washed in 2% FCS. Red blood cells were lysed using ACK lysis buffer and the pellet was then resuspended in FACS buffer.

Skin

The hairless part of the mouse ears was cut and the dorsal and ventral side were separated by pulling them apart with forceps. Any remaining cartilage was gently removed. The two sides were then minced and digested in RPMI containing 2 mg/ml collagenase type II (Sigma), 150 μg/ml DNase I (Sigma), and 0.5 mg/ml hyaluronidase (Sigma) for 50 min – with frequent vortexing (every 15 min). The dissociation lysat was filtered through a 40-μm cell strainer, washed with 2% FBS-RPMI and resuspended in FACS buffer.

Flow cytometry

Surface staining of the single cell suspensions was performed for 30 min at 4°C, and viability was assessed using LIVE/DEAD Fixable viability dye as per the manufacturer's instructions (Thermo Fisher Scientific).

The following surface markers antibodies from Biolegend were used: anti-CD3 (clone: 145-2C11), anti-CD4 (RM4-5), anti-CD8a (53–5.8), anti-CD45 (30-F11), anti-CD11b (M1/70), anti-CD11c (N418), anti-CD19 (6D5), anti-TCRβ (H57-597), anti-NK1.1 (PK136), anti-KLRG1 (2F1), anti-PD-1 (29F.1A12), anti-CD25 (PC-61), anti-CD44 (IM7), anti-CD62L (MEL-14), anti-Thy1.1 (OX-7), anti-CCR2 (SA203G11), anti-CXCR3 (CXCR3-173), anti-CXCR5 (L138D7), anti-CXCR6 (SA051D1), anti-CD103 (2E7). Samples were

then fixed overnight at 4°C using the using 100 μL of Foxp3 Fix/Perm buffer (eBioscience). After membrane permeabilization using 1X permeabilization buffer (eBioscience) for 5 min, intracellular staining was performed for 120 min at room temperature using the following antibodies: anti-Ctla-4 (UC10-4B9, Biolegend), anti-Helios (22F6, Biolegend), anti-Foxp3 (FJK16, Thermofisher), anti-Gata3 (TWAJ, Thermofisher), anti-RORγ (AFKJS-9, Thermofisher), anti-Ki-67 (16A8, Biolegend). Cells were acquired with an Aurora flow cytometer (Cytek Biosciences) or a FACSymphony flow cytometer (BD Biosciences). Data were analyzed using FlowJo software version 10 (TreeStar, BD LifeSciences).

Cell sorting for bulk RNAseq and scATACseq

Cells were sorted using BD MoFlo Astrios EQ, FACSAria-561, or FACSAria-594 machines.

For Bulk RNAseq, male mutant Tregs were sorted as aTreg (DAPI$^-$ CD19$^-$ TCRb$^+$ CD4$^+$ CD25^{hi} CD44^{hi} CD62L^{lo}) or rTreg ((DAPI$^-$ CD19$^-$ TCRb$^+$ CD4$^+$ CD25^{hi} CD44$^-$ CD62L$^+$). Female mutant Tregs were sorted as aTreg (DAPI$^-$ CD19$^-$ TCRb$^+$ CD4$^+$ Thy1.1$^-$ CD25^{hi} CD44^{hi} CD62L^{lo}) or rTreg ((DAPI$^-$ CD19$^-$ TCRb$^+$ CD4$^+$ Thy1.1$^-$ CD25^{hi} CD44$^-$ CD62L$^+$). Tconv (when applicable) were sorted as DAPI$^-$ CD19$^-$ TCRb$^+$ CD4$^+$ CD25$^-$. For mutations inserted into the Foxp3$^{ires.GFP}$ background, the Treg purity was checking using the GFP channel: 99–100% for the rTreg compartment and 94–96% for the aTreg compartment. For scATAC seq, we used the same gating strategy, except that for the mutations inserted into the Foxp3$^{ires.GFP}$ background, we also added a "GFP+" gate, increasing the purity (Figure S7A).

Bulk RNA-seq library preparation

BulkRNA-seq analyses were perfomed in mutant males and heterozygous females (cf. above the sorting strategy). 1000 cells of each population were directly double-sorted into 5 μL TCL buffer (Qiagen) supplemented with 1% 2-mercaptoethanol (Sigma) for cell lysis. Samples were then processed into Smart-seq2 RNA-seq library preparation and sequencing by the Broad Genomics Platform, following the standard ImmGen ultra-low-input RNA-seq protocol (immgen.org).

Bulk RNA-seq pre-processing and analysis

Reads were aligned to the GRCm38 - mm10 genome by STAR and counts quantified using featureCounts (Subread). Samples with fewer than 8,000 genes with more than ten reads, high contamination by hematopoietic-cell-specific transcripts, median transcript integrity number for housekeeping genes below 45, or poor intra-replicate correlation were excluded from downstream analyses.

Software

All transcriptomic analyses were performed using R studio software (v2022.12.0 + 353), and visualizations were generated using R studio software (v2022.12.0 + 353) or GraphPad Prism software (v9.5.0).

Filtering data

Genes with a minimum read count of 15 in all replicates for each specific population (i.e., rTreg male C168Y) were retained for the downstream comparisons.

Differentially expressed genes

We used an uncorrected t test to estimate the significance of differential gene expression between the different groups from the normalized read counts dataset. Genes with a FoldChange >2 or <0.5 and p value <0.01 were selected for further analysis. For each comparison, a population was compared to a pool of WT from the same state (rTreg or aTreg), the same sex (male or female) and the same background (straight B6 or B6.Foxp3$^{ires.GFP}$)

Selection of R51Q, K199del and R309Q specific genes

These genesets were extracted from the FoxP3-dependent gene signature from,[20] displayed in Table S2. Then they were further refined based on the concordance between the rTreg and aTreg datasets for K199del and R309Q, and between the reTreg from B6 and B6.Foxp3$^{ires.GFP}$ for R51Q (FoldChange in both setting less than 0.75 and at least in one of them less than 0.66)

Transcriptomic scores

The *Hill* Up and *Scurfy* Up scores were similarly calculated. Briefly, the average FoldChange of the up-signature genes from the respective signature was calculated for each replicate. The values were then normalized into a specific scale, where 0 corresponded to the average value in Tconv for the Hill Up and in WT Treg for Scurfy Up, and 1 corresponded to the average value in WT Treg for the Hill Up and in Scurfy Treg for Scurfy Up.

Comparison to published datasets

For published datasets, count matrices were downloaded directly through GEO and used for differential expression analyses. We used the following dataset GSE154680[20], GSE89654[30] (Table S2).

scATAC-seq library preparation

Nuclei isolation, transposition, GEM generation, and library construction targeting capture of 10000 cells were carried out as detailed in the Chromium Next GEM Single Cell ATAC manual (10x Genomics) with modifications to allow sample hashtagging (see "scATAC Hashtagging (ASAP-seq)" below). Libraries were pooled and sequenced on an Illumina NovaSeq 6000 to a final median depth of approximately 20–30,000 paired-end reads per cell. Sequencing data were converted to fastq files, aligned to the mm10 reference genome, and quantified per cell using Cell Ranger ATAC software (10x Genomics, v1.2).

scATAC hashtagging (ASAP-seq)

To include multiple experimental conditions in the same scATAC run, we hashtagged cells using a modification of the ASAP-seq strategy[59] for low cell input primary cell samples. Before sorting, cells were hashtagged with mouse TotalSeqA DNA-barcoded hashtag antibodies at the same time as staining with fluorophore-conjugated antibodies (BioLegend). Hashtags used are provided in Table S5. Cells were sorted into DMEM +5% FCS in DNA Lo-Bind tubes (Eppendorf, cat # 022431021). After spinning down for 5 min at 500g in a refrigerated centrifuge at 4°C, cells were resuspended in 100 μL chilled 0.1x Omni Lysis buffer (1x Omni Lysis buffer (10mM Tris-HCl, 10mM NaCl, 3 mM $MgCl_2$, 0.1% Tween 20, 0.1% NP40 substitute/IGEPAL, 0.01% Digitonin, 1% BSA in nuclease free water) diluted 1:10 in Wash/Lysis Dilution Buffer (10mM Tris-HCl, 10mM NaCl, 3 mM $MgCl_2$, 1% BSA in nuclease free water), gently mixed by pipetting, and incubated on ice for 6.5 min. Following lysis, 100 μL chilled wash buffer was added and gently mixed by pipetting. Cells were spun down for 5 min at 500 g at 4°C, all but 5 μL of supernatant was removed, and 45 μL of chilled 1x nuclei buffer (10x Genomics) was added without mixing. After one more centrifugation step at 500g, 4°C for 5 min, supernatant was removed, and samples were resuspended in 7ul 1x nuclei buffer for cell counting and input into transposition, barcoding, and library preparation according to the Chromium Next GEM Single Cell ATAC manual (10x Genomics).

Modifications to the original 10X protocol were made as described in the original ASAP-seq publication and as detailed at https://citeseq.files.wordpress.com/2020/09/asap_protocol_20200908.pdf. Briefly, 0.5 μL of 1uM BOA bridge oligo was spiked into the barcoding reaction. During GEM incubation, an additional 5 min incubation at 40°C was added to the beginning of the protocol. 43.5 instead of 40.5 μL of Elution Solution I was added during silane bead elution to recover 43 μL. 40 μL was used for SPRI clean up as indicated in the protocol, while 3 μL was set aside. During SPRI cleanup, the supernatant was saved. The bead bound fraction was processed as in the protocol, while for the supernatant fraction, 32 μL SPRI was added for 5 min. Beads were collected on a magnet, washed twice with 80% ethanol, and eluted in 42 μL EB. This 42 μL was combined with the 3 μL set aside from the previous step as input into the HTO indexing reaction. HTO Indexing PCR was run with partial P5 and indexed Rpxx primers (https://citeseq.files.wordpress.com/2020/09/asap_protocol_20200908.pdf) as: 95°C 3 min, 12–14 cycles of (95°C 20 s, 60°C 30 s, 72°C 20 s), 72°C 5 min. The PCR product was cleaned up with 1.6X SPRI purification for quantification and sequencing alongside ATAC libraries.

scATAC-seq preprocessing and visualization

Data analysis was performed using Signac v1.4[77]. For quality control, only cells with at least 1×10^3 fragments per cell (depending on sequencing depth of experiment), greater than 50 percent reads in peaks, TSS enrichment score greater than 2, nucleosome signal less than 10, and ratio of blacklist-region reads less than 0.05 were retained for further analysis. Putative doublets identified by ArchR v1.0.1[76] and non-Treg, non-Tconv contaminant cells were also removed. We used the latent semantic indexing approach as previously described[82,83]. Binarized count matrices were normalized using the term frequency-inverse document frequency (TF-IDF) transformation and reduced in dimensionality by singular value decomposition (SVD). As the first component was highly correlated with sequencing depth, SVD components 2–30 were used to generate a shared nearest neighbor (SNN) graph for clustering and as input into UMAP[84] with cosine distance metric for visualization.

scATAC-seq analysis

Hashtag counts + assignments

Hashtag processing followed the original recommendations of the ASAP-seq paper[59], using asap_to_kite (https://github.com/caleblareau/asap_to_kite) to process FASTQs files for downstream quantification by the bustools and kite workflows.[85,86] We used the HTODemux()[87] function in the Seurat package (v4.0.2)[78] to remove doublets and call hashtag identities.

Peak sets

To enable comparisons across conditions and datasets, we used a common set of Treg-specific open chromatin regions, defined previously[43] by supplementing pan-immunocyte OCRs from the ImmGen consortium[88] with additional peaks from Treg scATAC-seq data.

Motif accessibility analysis

Bias-corrected relative motif accessibility was calculated using chromVAR.[60] We used motifmatchr (https://github.com/GreenleafLab/motifmatchr) to scan OCRs in our refence set from the curated set of mouse motif PWMs from the Buenrostro lab (https://github.com/buenrostrolab/chromVARmotifs/tree/master/data/mouse_pwms_v2.rda).

Gene scores

Gene scores were calculated with Archr v1.0.1, using an exponentially weighted function that accounts for the activity of distal OCRs in a distance-dependent manner[76] and provides an approximate proxy for gene expression.

Pseudobulk track visualization

To visualize pseudobulk profiles, BAM files containing reads for each group of cells were extracted using Sinto (https://github.com/timoast/sinto), shifted to account for Tn5 cut-sites, and converted to bigwigs using deeptools[79] for display in the Integrative Genomics Viewer[80].

Differential accessibility

We calculated differential accessibility between FoxP3 mutant and WT cells (GFP WT for R51Q and K199del and B6 WT sorted on $CD25^+$ population for R337Q) by using a logistic regression per OCR with number of fragments per cell included as a latent variable. To avoid effects driven by cell composition, we computed differentials separately between clusters corresponding to rTregs and aTregs. OCRs with average $|\log_2$ Fold Change$| > 0.1$ and p value <0.05 were designated as differential. In the case of the full KO comparison, we computed log2FC between quantile-normalized aggregated scATAC pseudobulk profiles from GFP^+ FoxP3 KO ($Foxp3^{fs327}$-GFP/Foxp3-Thy1.1) or GFP^+ WT ($Foxp3^{wt}$-GFP/Foxp3-Thy1.1) cells from a previous study[43].

Motif enrichment

To calculate enrichment of motifs within differential OCRs, we used a permutation testing framework. We compared the number of observed motif matches within each OCR set to the number of matches among a set of 100 background OCRs matched for GC content and accessibility (chosen using the chromVAR getBackgroundPeaks() function). Significance was assessed using a two-sided Z test, with Benjamini-Hochberg false discovery rate correction. We kept motif enrichments with FDR $< 1 \times 10^{-3}$.

OCR signature relative accessibility

Per-cell relative accessibility of OCR sets, including signature OCRs, TF binding sites, etc, was calculated using the chromVAR computeDeviations() function[60].

QUANTIFICATION AND STATISTICAL ANALYSIS

All statistical analyses were performed using R studio software (v2022.12.0 + 353), Python software (v3.9.7) or GraphPad Prism (v9.5.0) software. If not stated otherwise, data were presented as mean ± SD, statistical significance was calculated by a Mann-Whitney test. Except for selection of differential expressed genes (cf. above), $p < 0.05$ was considered significant. P-values for gene signature enrichment either up or down in volcano plots were determined using the $\chi 2$ test, relative to a 50/50 null distribution (behavior of the signature in the selected dataset versus the signature in a dataset where 50% of the genes would be represented in either side of the volcano plot).